



Vibrations of cracked rectangular FGM thick plates

C.S. Huang^{a,*}, O.G. McGee III^b, M.J. Chang^c

^a Department of Civil Engineering, National Chiao Tung University, 1001 Ta-Hsueh Rd., Hsinchu, Taiwan 30050, People's Republic of China

^b Department of Mechanical Engineering, Howard University, Washington, DC, USA

^c Institute of Nuclear Energy Research, Atomic Energy Council, 3-21 No. 1000, Wenhua Rd., Jiaan Village, Longtan Township, Tauhuang, Taiwan 32546, People's Republic of China

ARTICLE INFO

Article history:

Available online 14 January 2011

Keywords:

Ritz method
Higher-order shear deformable plate theory (HOSDPT)
Side-cracked plates
Functionally graded material (FGM)
Crack functions

ABSTRACT

Accurate first-of-its-kind solutions of the free vibration characteristics of side-cracked rectangular functionally graded material (FGM) thick plates are reported. From a brief review summary of available shear deformable plate theories, the well-established Reddy third-order plate theory apropos to cracked FGM thick plates is utilized. A novel Ritz procedure is developed incorporating special admissible functions – appropriately named in this study as *crack functions* – that properly account for the stress singularity behaviors in the neighborhood of a crack tip, and that properly account for the discontinuities of displacements and slopes across a crack. Material properties of the FGM plates are assumed to vary continuously in the thickness direction according to the Mori–Tanaka scheme or a simple power law. The proposed special admissible functions accelerate the convergence of the extensive non-dimensional frequency solutions summarized. The first known non-dimensional frequencies of simply-supported and cantilevered cracked aluminum (Al) and ceramic (zirconia (ZrO₂)) or alumina (Al₂O₃) FGM thick plates of moderate thickness ratio (side-length to plate thickness, $b/h = 10$) are accurately determined. The effects of the volume fraction in the modeling of material distribution in the thickness direction and of cracks with different lengths, locations and orientations on the non-dimensional frequencies are investigated.

© 2011 Elsevier Ltd All rights reserved.

1. Introduction

Materials with microstructures that vary over a macroscopic length scale are defined as functionally graded materials (FGMs) [1]. They are found in biological systems such as human and animal bones [2]. Man-made FGMs were first developed in the mid-1980s [3]. Continuously changing microstructures of FGMs make their mechanical properties better than those of traditional laminated composite materials, which are prone to debonding along the layer interfaces, caused by abrupt changes in the material properties. To satisfy the requirements of various applications and work environments, gradual changes of the material properties in FGMs are designed by controlling the volume fractions of two or more materials in manufacture. In the most recent two decades, FGMs have been extensively explored in a variety of fields, including electronics, chemistry, optics, biomedicine, aeronautical and mechanical engineering.

Plates are employed in a wide range of mechanical and structural system components in civil, mechanical and aeronautical engineering. Much of the published research reviewed on FGM plates [4,5] is devoted to addressing thermal problems with a num-

ber of efforts devoted to the vibrations of FGM plates contrasting the extensive amount of work devoted to free vibration studies of isotropic and homogenous plates or laminated composite plates. Based on classical Kirchhoff thin plate theory, Yang and Shen [6] studied the vibrations of fully clamped FGM square plates with initial in-plane stresses, and He et al. [7] examined the vibrations of FGM square plates with integrated piezoelectric sensors and actuators. Zhao et al. [8] adopted a first-order shear deformable plate theory to analyze the vibrations of FGM square plates under various boundary conditions. Developing a third-order shear deformable theory, Reddy [9] presented a finite element solution for the dynamic analysis of a FGM plate, and Ferreira et al. [10] employed an emerging meshless local Petrov–Galerkin formulation to solve the governing FGM plate equations of motion. Using two-dimensional higher-order plate theory, Matsunaga [11] developed a set of fundamental dynamic equations and presented analytical solutions for simply-supported rectangular plates, while Qian et al. [12] utilized a meshless local Petrov–Galerkin method to solve the governing equations of higher-order shear and normal deformable plate theory and to elucidate the static deformation and vibration behaviors of square plates. Vel and Batra [13] proposed three-dimensional solutions for vibrations of simply-supported rectangular plates.

Side-cracked FGM plates have not been previously investigated in the published literature even though such plates may have

* Corresponding author. Tel.: +886 3 5712121x54962; fax: +886 3 5716257.

E-mail addresses: cshuang@mail.nctu.edu.tw (C.S. Huang), ogmgee@yahoo.com (O.G. McGee), mjchang@iner.gov.tw (M.J. Chang).

cracks after they are subjected to large cyclic loading leading to fatigue and material flaws, including the initiation and growth of inter-laminar cracks in FGM plates (which are not a considered focus of this analysis albeit important one nonetheless). The main purpose of this work is to propose accurate first-of-its-kind solutions for the vibrations of side-cracked FGM thick plates, modeled using the well-known Reddy third-order shear deformable plate theory [14], and to elucidate the effects of material properties and side cracks on the vibration behaviors of such plates.

An interesting question has been now resolved as to whether stresses in the vicinity of a reentrant corner vertex or crack tip or discontinuous interface of two materials actually tends to infinity or whether this is a result of any inadequacies of classical Kirchhoff thin plate, first-order shear deformable plate, higher-order shear deformable plate, or three-dimensional elasticity-based theories. One might suppose that the stress singularities in the various problems examined in this body of work are just a mathematical nuance that might disappear physically, if rather closer considerations were given to the associated boundary conditions or the governing differential equations of motion. Max Williams in his classical 1951 work examined Reissner's shear deformable complementary energy-based theory to define the nature of the stress singularity at a crack tip, showing such stress singularities to be unaltered, when in addition to zero displacement and normal moment, there is zero rotation at a simply-supported edge of thin or even moderately thick plates.

Of particular interest to civil, mechanical, and aeronautical engineers nowadays is the more specific nature of stress singularities which indeed occur in cracked thick plates. Like in homogenous and isotropic thin and thick plates having a side crack, FGM cracked thick plates similarly have stress singularities at the crack tip [15]. The behaviors of stress singularities in the neighborhood of the crack tip should be taken into account in an accurate analysis. This work employed an analogous methodology used by Huang and Leissa [16] for studying the vibrations of a homogenous and isotropic plate with a side crack based on the classical plate theory. The present work utilizes third-order shear deformable plate theory in a novel Ritz procedure incorporating admissible functions

that explicitly account for bending moment and shear stress singularities at the crack tip and for the continuity of bending displacements and rotations across a side crack in a rectangular FGM thick plate. The robustness of the proposed Ritz procedure in providing accurate numerical solutions depends strongly on the use of the constructed hybrid series of admissible functions used. Essentially, the admissible functions for each in-plane and out-of-plane displacement components consist of two sets of trial functions. It was shown by Ritz in his original memoir [17] that it is advantageous if a possible set of trial functions are chosen so that they form an orthogonal set. Accordingly, the first set used in the present analysis is a mathematically complete set of orthogonal polynomials. It was also shown by Ritz in his 1908 original work that sometimes the functions occurring in the exact solution of one problem may be used in the approximate solution of another. Consequently, the other is a set of functions to approximate the solution of the titled problem are derived from an exact solution to the singular behaviors of stresses at the tip of a crack, including the discontinuities of the displacements and their derivatives across the crack. The effects of the proposed hybrid series in determining the natural frequencies of side-cracked FGM plates are demonstrated through comprehensive convergence studies. New and accurate vibration data of simply-supported and cantilevered moderately thick plates with side cracks having various locations (c_x or c_y), lengths (d) and orientations (α) (Fig. 1) are reported. Notably, when a crack closes and may causes two sides of the crack to collide with each other during vibration, it is a complicate nonlinear phenomenon, and not considered in the present study.

2. Method of analysis

2.1. Ritz procedure for cracked FGM thick plate vibrations

Thick FGM plates are ones with a thickness larger by approximately one order of magnitude when compared with the characteristic length or the plate's vibration mode shape wavelength (thickness is larger than a tenth of the smallest wavelengths). Thick plate theories incorporate shear deformation and rotary inertia in

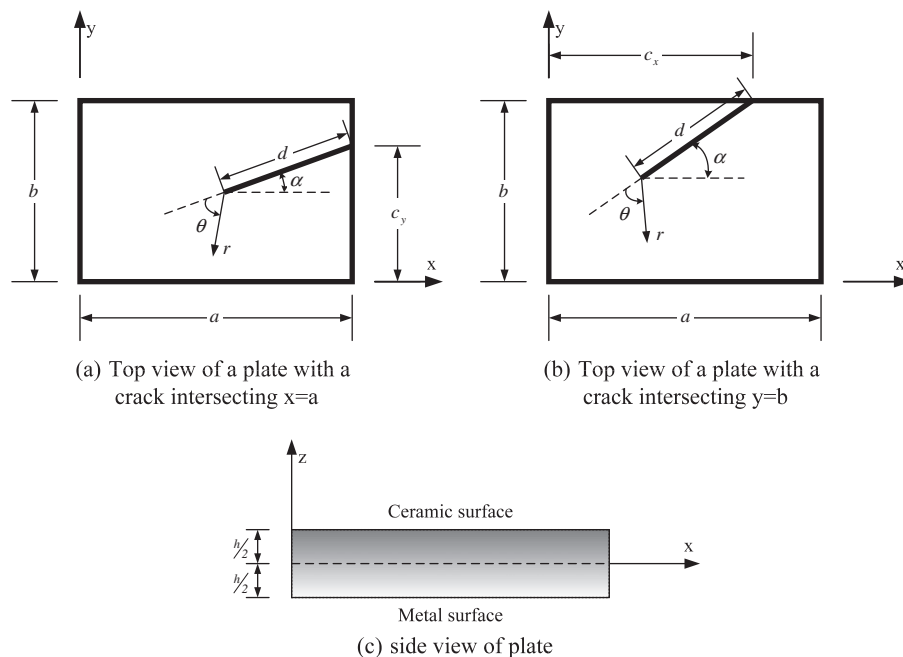


Fig. 1. A functionally graded material plate with a side crack.

the assumed displacement approximations, creating consistent equations applicable to development of a Ritz procedure for cracked FGM thick plate vibrations. Widely documented in the literature are numerous displacement-based shear deformable plate theories applicable to cracked FGM thick plate vibrations [18–45], which are briefly summarized in Appendix I. The various theories chronicled in the previous scholarship [46,47] largely spans across Mindlin, Reissner, and Ambartsumyan approaches, which are typically adequate for flexural bending and vibration frequency solutions for FGM thick plates. The summaries of these various theories given in Tables A.I.1–A.I.3 provide a brief review of the associated literature and some justification and relative perspective as to the choice of higher-order shear deformable assumed displacement approximation adopted in the present study. The present Reddy HOSDPT approach adopted in this study is a Henchy–Mindlin-based approach, which corrects upon a similar Henchy–Mindlin approach of Kant [34] by subtracting cubic-order terms through the FGM plate thickness proportional to sums of first-order bending rotations and transverse normal strains. Such a HOSDPT displacement field approximation was adopted to sufficiently account for transverse shear flexibilities adequately, while augmenting the approximation to address transverse shear and normal stress singularities at a side crack in the upper bound Ritz frequency calculations. This third-order shear deformable plate theory originally proposed by Reddy [14,32,33] is adopted to analyze the vibrations of FGM plates with side cracks. The displacement components (u , v and w) in the x , y and z directions, respectively, are assumed as

$$\begin{aligned} u(x, y, z, t) &= u_0(x, y, t) + z\phi_x(x, y, t) - \frac{4z^3}{3h^2} \left(\phi_x(x, y, t) + \frac{\partial w_0(x, y, t)}{\partial x} \right), \\ v(x, y, z, t) &= v_0(x, y, t) + z\phi_y(x, y, t) - \frac{4z^3}{3h^2} \left(\phi_y(x, y, t) + \frac{\partial w_0(x, y, t)}{\partial y} \right), \\ w(x, y, z, t) &= w_0(x, y, t), \end{aligned} \tag{1}$$

where u_0 , v_0 and w_0 denote the components of displacement of a point on the plane $z = 0$; ϕ_x and ϕ_y are the angles of rotation of the transverse normal about the y and x axes, respectively; h is the plate thickness, and t is time.

Assuming the temporal motion is simple harmonic,

$$\begin{aligned} u_0(x, y, t) &= U(x, y)e^{i\omega t}, & v_0(x, y, t) &= V(x, y)e^{i\omega t}, \\ w_0(x, y, t) &= W(x, y)e^{i\omega t}, & \phi_x(x, y, t) &= \Phi_x(x, y)e^{i\omega t}, \\ \phi_y(x, y, t) &= \Phi_y(x, y)e^{i\omega t}, \end{aligned} \tag{2}$$

one defines ω as the plate’s vibratory circular frequency. Substituting Eqs. (1) and (2) into the equations for strain energy and kinetic energy in Reddy’s plate theory, one obtains the maximum strain energy (V_{max}) and the maximum kinetic energy (T_{max}) required in the energy functional statement minimized in the Ritz method,

$$\begin{aligned} U_{max} &= \frac{1}{2} \int \int_A \left\{ [\bar{A}_{11}U_x + 2\bar{K}_{11}\Phi_{xx} - 2C_1\bar{E}_{11}W_{xx} + 2\bar{A}_{12}V_y + 2\bar{K}_{12}\Psi_{yy} \right. \\ &\quad - 2C_1\bar{E}_{12}W_{yy}]U_x + [\bar{A}_{44}(U_y + 2V_x) + 2\bar{K}_{44}(\Phi_{xy} + \Phi_{yx}) \\ &\quad - 4C_1\bar{E}_{44}W_{xy}]U_y + [\bar{A}_{44}V_x + 2\bar{K}_{44}(\Phi_{xy} + \Phi_{yx}) \\ &\quad - 4C_1\bar{E}_{44}W_{xy}]V_x + [2\bar{K}_{12}\Phi_{xx} - 2C_1\bar{E}_{12}W_{xx} + \bar{A}_{11}V_y \\ &\quad + 2\bar{K}_{11}\Phi_{yy} - 2C_1\bar{E}_{11}W_{yy}]V_y + (\bar{M}_0 - C_2\bar{M}_2)(\Phi_x + 2W_x)\Phi_x \\ &\quad + (\bar{J}_{11} - C_1\bar{L}_{11})\Phi_{xx} - 2C_1\bar{L}_{11}W_{xx} + 2(\bar{J}_{12} - C_1\bar{L}_{12})\Phi_{xy} \\ &\quad - 2C_1\bar{L}_{12}W_{yy}]\Phi_{xx} + (\bar{J}_{44} - C_1\bar{L}_{44})(\Phi_{xy} + 2\Phi_{yx}) - 4C_1\bar{L}_{44}W_{xy}\Phi_{xy} \\ &\quad + (\bar{M}_0 - C_2\bar{M}_2)(\Phi_y + 2W_y)\Phi_y + (\bar{J}_{44} - C_1\bar{L}_{44})\Phi_{yx} - 4C_1\bar{L}_{44}W_{xy}\Phi_{yx} \\ &\quad + [-2C_1\bar{L}_{12}W_{xx} + (\bar{J}_{11} - C_1\bar{L}_{11})\Phi_{yy} - 2C_1\bar{L}_{11}W_{yy}]\Phi_{yy} \\ &\quad + (\bar{M}_0 - C_2\bar{M}_2)(W_x^2 + W_y^2) + [C_1^2(\bar{H}_{11}W_{xx} + \bar{H}_{12}W_{yy})]W_{xx} \\ &\quad \left. + [C_1^2(\bar{H}_{12}W_{xx} + \bar{H}_{11}W_{yy})]W_{yy} + 4C_1\bar{H}_{44}[W_{xy}]^2 \right\} dA \end{aligned} \tag{3a}$$

$$\begin{aligned} T_{max} &= \frac{\omega^2}{2} \int \int \int \rho \left\{ [U + z\Phi_x - C_1z^3(\Phi_x + W_x)]^2 \right. \\ &\quad \left. + [V + z\Phi_y - C_1z^3(\Phi_y + W_y)]^2 + W^2 \right\} dz dA \end{aligned} \tag{3b}$$

where $(\bar{A}_{ij}, \bar{B}_{ij}, \bar{D}_{ij}, \bar{E}_{ij}, \bar{F}_{ij}, \bar{H}_{ij}) = \int_{-h/2}^{h/2} Q_{ij}(1, z, z^2, z^3, z^4, z^6) dz$,

$$\begin{aligned} \bar{K}_{ij} &= \bar{B}_{ij} - C_1\bar{E}_{ij}, & \bar{J}_{ij} &= \bar{D}_{ij} - C_1\bar{F}_{ij}, & \bar{L}_{ij} &= \bar{F}_{ij} - C_1\bar{H}_{ij}, \\ \bar{I}_k &= \int_{-h/2}^{h/2} Q_{44}z^k dz, & \bar{M}_k &= \bar{I}_k - C_2\bar{I}_{k+2} \quad (ij = 11, 12, \text{ or } 44; \text{ and } k = 0 \text{ or } 2) \\ C_1 &= \frac{4}{3h^2}, & C_2 &= 3C_1, & Q_{11} &= \frac{E}{1-\nu^2}, & Q_{12} &= \nu Q_{11}, & Q_{44} &= \frac{E}{2(1+\nu)}, \end{aligned}$$

E , ν and ρ are the Young’s modulus, Poisson’s ratio, and mass per unit volume of the plate, respectively. (In the above the subscripted comma indicates partial differentiation with respect to the coordinate indicated by the variable following the comma.)

The vibration frequencies of the plate are obtained by minimizing the energy functional

$$\Pi = V_{max} - T_{max}. \tag{4}$$

Let the spatial in-plane and transverse displacements and transverse bending rotations in Eq. (2) be approximated as a hybrid series of admissible functions, satisfying the geometric boundary conditions on the displacements and rotations of the shear deformable thick plate, as follows:

$$\begin{aligned} U(x, y) &= \sum_{i=1}^{\infty} a_i \xi_i(x, y), & V(x, y) &= \sum_{i=1}^{\infty} b_i \zeta_i(x, y), \\ W(x, y) &= \sum_{i=1}^{\infty} e_i \varphi_i(x, y), & \Phi_x(x, y) &= \sum_{i=1}^{\infty} d_i \chi_i(x, y), \\ \Phi_y(x, y) &= \sum_{i=1}^{\infty} c_i \eta_i(x, y) \end{aligned} \tag{5}$$

where a_i , b_i , c_i , d_i , and e_i are undetermined generalized coefficients. For a rectangular thick plate with a side crack (see Fig. 1), each of the displacement and rotation functions U , V , W , Φ_x and Φ_y is assumed as a hybrid series comprised of two sets of functions:

$$\begin{aligned} U &= \Psi_{1p} + \Psi_{1c}, & V &= \Psi_{2p} + \Psi_{2c}, & W &= \Psi_{3p} + \Psi_{3c}, \\ \Phi_x &= \Psi_{4p} + \Psi_{4c}, & \Phi_y &= \Psi_{5p} + \Psi_{5c}, \end{aligned} \tag{6}$$

where the sets of functions indicated by the subscript “ p ” consist of orthogonal polynomials, which form a mathematically complete set, if an infinite number of terms are used, and the sets of functions indicated by the subscript “ c ” are to supplement the polynomials by characterizing the important features of the exact solutions along the crack.

The set of orthogonal polynomials used in Eq. (6) are written as follows:

$$\Psi_{kp}(x, y) = \sum_{i=1}^{I_k} \sum_{j=1}^{J_k} a_{ij}^{(k)} P_{ki}(x) Q_{kj}(y), \quad (k = 1, 2, \dots, 5), \tag{7}$$

where $P_{ki}(x)$ and $Q_{kj}(y)$ are sets of orthogonal polynomials in the x and y directions of the rectangular plate under consideration (Fig. 1). These orthogonal polynomials are generated by using a Gram–Schmidt process [44] and satisfy the geometric boundary conditions of the rectangular FGM thick plate under consideration.

Clearly, the polynomials in Eq. (7) do not reveal the presence of a side crack. To enhance the effectiveness of the proposed Ritz procedure in identifying a side crack, sets of functions that describe the important features of such a crack have been developed. They are

$$\Psi_{kc}(r, \theta) = g_k(x, y) \left(\sum_{n=1}^{\bar{N}_{1k}} \sum_{l=0}^n b_{nl}^{(k)} r^{(2n-1)/2} \cos \frac{2l+1}{2} \theta + \sum_{n=1}^{\bar{N}_{2k}} \sum_{l=0}^n c_{nl}^{(k)} r^{(2n-1)/2} \sin \frac{2l+1}{2} \theta \right) \quad (\text{for } k = 1, 2, 4, \text{ and } 5), \quad (8a)$$

$$\Psi_{3c}(r, \theta) = g_3(x, y) \left(\sum_{n=1}^{\bar{N}_{13}} \sum_{l=0}^n b_{nl}^{(3)} r^{(2n+1)/2} \cos \frac{2l+1}{2} \theta + \sum_{n=1}^{\bar{N}_{23}} \sum_{l=0}^n c_{nl}^{(3)} r^{(2n+1)/2} \sin \frac{2l+1}{2} \theta \right), \quad (8b)$$

where functions $g_i(x, y)$ are introduced to satisfy the geometric boundary conditions along $x = 0$, $x = a$, $y = 0$, and $y = b$, and the origin of the (r, θ) coordinate system is at the crack tip (Fig. 1). The proposed functions in Eqs. (8) are developed from the asymptotic solutions presented by Huang and Chang [15]. The asymptotic solutions in the neighborhood of a crack tip depend linearly on the functions in Eqs. (8), if $g_i(x, y)$ are set equal to unity. Notably, Eqs. (8) with $n = 1$ yields the exact singularity orders of stress resultants at the crack tip [15]. The sine and cosine functions result in discontinuities of functions in both the functions themselves and their gradients across the crack. The functions in Eqs. (8) are appropriately named in this study as *crack functions*.

Substituting Eq. (5) into Eqs. (3) and (4) and minimizing the energy functional (Eq. (4)) with respect to the generalized coefficients of Eq. (5) leads to the following matrix set of linear homogeneous algebraic equations,

$$\begin{bmatrix} K^{11} & K^{12} & K^{13} & K^{14} & K^{15} \\ & K^{22} & K^{23} & K^{24} & K^{25} \\ & & K^{33} & K^{34} & K^{35} \\ \text{sym.} & & & K^{44} & K^{45} \\ & & & & K^{55} \end{bmatrix} \begin{Bmatrix} a_i \\ b_i \\ c_i \\ d_i \\ e_i \end{Bmatrix} = \omega^2 \begin{bmatrix} M^{11} & M^{12} & M^{13} & M^{14} & M^{15} \\ & M^{22} & M^{23} & M^{24} & M^{25} \\ & & M^{33} & M^{34} & M^{35} \\ \text{sym.} & & & M^{44} & M^{45} \\ & & & & M^{55} \end{bmatrix} \begin{Bmatrix} a_i \\ b_i \\ c_i \\ d_i \\ e_i \end{Bmatrix}, \quad (9)$$

which is expressed in the form of a standard eigenvalue problem – the eigenvalues being the circular frequencies of vibration of the plate. Explicit expressions of the matrix coefficients, K^{ij} and M^{ij} are given in Appendix II. The associated eigenvectors $\{a_i, b_i, c_i, d_i, e_i\}^T$ may be substituted back into Eqs. (5) in order to obtain the plate vibration mode shapes corresponding to the circular frequencies of vibration. In the numerical studies of this analysis, \bar{N}_{1k} and \bar{N}_{2k} in Eqs. (8) are set equal to a common value, \bar{N} , and I_k and J_k in Eq. (7) are set to corresponding common values, I and J , respectively, for $k = 1, 2, \dots, 5$. Consequently, the use of the admissible functions given by Eqs. (7) and (8) yields a total number of $5 \times [(I \times J) + \bar{N} \times (\bar{N} + 3)]$ equations characterizing the algebraic solution Eqs. (9).

2.2. Functionally graded material (FGM) properties

Based on the assumption that an FGM plate comprises two randomly distributed isotropic constituents, the macroscopic response of the plate is isotropic, and the material properties of the plate vary only in the thickness direction. Two models have been commonly adopted in describing the variation of material properties along the thickness of the plate in literature on the vibrations of FGM plates. The effective material properties, generically represented as $P(z)$, representing the FGM thick plate elastic modulus, E , or Poisson's ratio, ν , or mass density, ρ , are assumed to be expressed as

Table 1
Material properties of the FGM components.

Material	Properties		
	E (GPa)	Poisson's ratio	ρ (kg/m ³)
Aluminum (Al)	70.0	0.3	2702.
Alumina (Al ₂ O ₃)	380.	0.3	3800.
Zirconia (ZrO ₂)	200.	0.3	5700.

$$P(z) = P_b + V(z)\Delta P \quad (10)$$

where $V(z) = (z/h + 1/2)^{\hat{n}}$; P_b denotes the properties at the bottom plate face ($z = -h/2$); ΔP is the difference between P_b and the corresponding property at the top plate face ($z = h/2$); h is plate thickness, and \hat{n} is the parameter that governs the material variation profile in the thickness direction.

The other model is based on the Mori–Tanaka scheme [45,46]. The effective mass density at a point in the plate is given by

$$\rho(z) = \rho_1 V_1(z) + \rho_2 V_2(z), \quad (11a)$$

$$V_1(z) + V_2(z) = 1, \quad (11b)$$

$$V_1(z) = V_1^- + (V_1^+ - V_1^-) \left(\frac{z}{h} + \frac{1}{2} \right)^{\hat{n}}, \quad (11c)$$

where subscripts 1 and 2 indicate materials 1 and 2, respectively, and V_1^+ and V_1^- are the volume fraction of material 1 on the top and the bottom surfaces of the plate, respectively. The effective local bulk modulus K and the shear modulus G are given by

$$\frac{K(z) - K_1}{K_2 - K_1} = \frac{V_2(z)}{1 + \frac{(K_2 - K_1)V_1(z)}{K_1 + (4/3)G_1}}, \quad \frac{G(z) - G_1}{G_2 - G_1} = \frac{V_2(z)}{1 + \frac{(G_2 - G_1)V_1(z)}{G_1 + f_1}} \quad (12)$$

where $f_1 = \frac{G_1(9K_1 + 8G_1)}{6(K_1 + 2G_1)}$. After the effective moduli K and G are estimated, the effective Young's modulus and Poisson's ratio are obtained using

$$E(z) = \frac{9K(z)G(z)}{3K(z) + G(z)} \quad \text{and} \quad \nu(z) = \frac{3K(z) - 2G(z)}{2(3K(z) + G(z))}. \quad (13)$$

In the following, the FGM plates under consideration are made of aluminum (Al) and ceramic (zirconia (ZrO₂)) or alumina (Al₂O₃), whose material properties are given in Table 1. The top of the plate ($z = h/2$) is further assumed to be pure ceramic, and the bottom of the plate ($z = -h/2$) is pure aluminum. Consequently, Eq. (11c) is simplified to,

$$V_1(z) = \left(\frac{z}{h} + \frac{1}{2} \right)^{\hat{n}}. \quad (14)$$

Note that the Poisson's ratios of the material given in Table 1 are the same. In invoking Eq. (10), Poisson's ratio $\nu(z)$ along the thickness is assumed constant, whereas $\nu(z)$ is not constant, when invoking the Mori–Tanaka scheme in the present Ritz procedure.

3. Convergence studies

The present Ritz procedure guarantees upper-bound approximate solutions on the exact vibration frequencies of rectangular shear deformable FGM thick plates. These upper-bound solutions in the limit converge to the exact solution, as the number of appropriate admissible functions increases sufficiently. Convergence studies of simply-supported rectangular plates with or without side cracks (Fig. 1) were conducted herein to verify the accuracy of the solutions and demonstrate the effects of the crack functions on the solutions. The geometric boundary conditions for a simply-supported rectangular shear deformable FGM plate are

Table 2
Convergence of $\omega h \sqrt{\rho_m/E_m}$ for a simply supported square Al/ZrO₂ FGM plate having $h/a = 0.05$ and $\hat{n} = 1$.

Mode No.	Orthogonal polynomial solution size ($I \times J$)					Ferreira et al. * [10]	Reddy [9]
	5 × 5	7 × 7	9 × 9	10 × 10	11 × 11		
1	0.01548	0.01548	0.01548	0.01548	0.01548	(0.0148) [0.0147]	0.01548
2	0.03832	0.03821	0.03821	0.03821	0.03821	(0.0381) [0.0375]	0.03821
3	0.03832	0.03821	0.03821	0.03821	0.03821	(0.0382) [0.0375]	0.03821
4	0.06055	0.06040	0.06040	0.06040	0.06040	(0.0594) [0.0592]	0.06040
5	0.1007	0.07586	0.07493	0.07491	0.07491	(0.0754) [0.0749]	0.07491

* [] meshless local Petrov–Galerkin solutions using 11 × 11 uniformly-spaced collocation points, cf. Ferreira et al. [10].

*() meshless local Petrov–Galerkin solutions using 9 × 9 uniformly-spaced collocation points, cf. Ferreira et al. [10].

Table 3
Convergence of frequency parameters $\omega(b^2/h)\sqrt{\rho_c/E_c}$ for a simply-supported homogeneous rectangular thin plate with a horizontal side crack ($a/b = 2.0$, $h/b = 0.01$, $c_y/b = 0.5$, $d/a = 0.5$, $\alpha = 0^\circ$).

Mode No.	Crack functions \bar{N} (Eqs. (8))	Orthogonal polynomial solution size ($I \times J$)						Stahl and Keer* [47] Huang and Leissa* [16]
		4 × 4	5 × 5	6 × 6	7 × 7	8 × 8	9 × 9	
1(S)	0	3.733	3.733	3.732	3.732	3.732	3.732	[3.05]
	4	3.062	3.052	3.051	3.050	3.050	3.049	(3.053)
	5	3.056	3.050	3.050	3.049	3.049	3.049	
	6	3.053	3.050	3.049	3.049	3.048	3.048	
	7	3.051	3.049	3.049	3.048	3.048	3.047	
2(S)	0	6.503	5.980	5.979	5.971	5.971	5.971	[5.507]
	4	5.542	5.509	5.506	5.504	5.504	5.504	(5.506)
	5	5.533	5.506	5.504	5.503	5.503	5.503	
	6	5.527	5.505	5.503	5.503	5.503	5.503	
	7	5.525	5.504	5.503	5.503	5.503	5.503	
3(A)	0	12.42	12.42	9.794	9.794	9.702	9.702	[5.570]
	4	5.594	5.579	5.569	5.566	5.564	5.564	(5.570)
	5	5.574	5.565	5.562	5.562	5.560	5.560	
	6	5.565	5.563	5.561	5.560	5.559	5.559	
	7	5.562	5.561	5.560	5.559	5.558	5.557	
4(S)	0	15.80	12.73	12.73	12.68	12.68	12.68	[9.336]
	4	10.00	9.391	9.369	9.347	9.338	9.336	(9.336)
	5	9.759	9.345	9.341	9.333	9.331	9.330	
	6	9.686	9.338	9.334	9.331	9.330	9.330	
	7	9.653	9.336	9.332	9.330	9.330	9.329	
5(A)	0	18.03	14.97	14.97	14.92	14.92	14.92	[12.76]
	4	13.08	12.95	12.91	12.85	12.83	12.83	(12.78)
	5	12.82	12.79	12.78	12.77	12.77	12.77	
	6	12.77	12.76	12.76	12.76	12.76	12.76	
	7	12.76	12.76	12.76	12.76	12.76	12.76	

* [] results cf. Stahl and Keer [47]; *() results cf. Huang and Leissa [16].

$$\begin{aligned}
 u_0(x, 0, t) = 0, \quad \phi_x(x, 0, t) = 0, \quad u_0(x, b, t) = 0, \quad \phi_x(x, b, t) = 0, \\
 v_0(0, y, t) = 0, \quad \phi_y(0, y, t) = 0, \quad v_0(a, y, t) = 0, \quad \phi_y(a, y, t) = 0, \\
 w_0(x, 0, t) = 0, \quad w_0(x, b, t) = 0, \quad w_0(0, y, t) = 0, \quad w_0(a, y, t) = 0.
 \end{aligned}
 \tag{15}$$

Accordingly, the following boundary function, $g_i(x, y)$ ($i = 1, 2, \dots, 5$), are used in constructing the admissibility of the assumed displacement fields (Eqs. (8)) satisfying the geometric boundary conditions:

$$\begin{aligned}
 g_1(x, y) = g_4(x, y) = y(b - y), \quad g_2(x, y) = g_5(x, y) = x(a - x), \quad \text{and} \\
 g_3(x, y) = xy(a - x)(b - y).
 \end{aligned}
 \tag{16}$$

3.1. Intact square FGM plate

Table 2 summarizes the convergence studies of the first five non-dimensional frequencies for an intact square Al/ZrO₂ FGM

plate with $h/a = 0.05$ and $\hat{n} = 1$. The Mori–Tanaka scheme was adopted to determine the effective material properties. The admissible functions in Eqs. (8) were not required, because the problem under consideration involves no crack. The non-dimensional frequency parameter, $\omega h \sqrt{\rho_m/E_m}$, in which subscript “ m ” refers to “metal” (Al), is employed for comparing with previous results in the published literature. Table 2 also compares the results of Ferreira et al. [10], who applied the meshless local Petrov–Galerkin formulation to solve the governing equations incorporating the present Reddy third-order shear deformable plate theory. The Ferreira et al. [10] meshless local Petrov–Galerkin solutions in parentheses were obtained using 9 × 9 uniformly-spaced collocation points, while those in brackets were obtained using 11 × 11 uniformly-spaced collocation points. The results of Reddy [9] were recomputed using his analytical solutions but with the simple modification of considering coupling between in-plane displacement components (u_0 and v_0) and rotation components (ϕ_x and ϕ_y) in the mass matrix.

Table 4
Convergence of frequency parameters $\omega(b^2/h)\sqrt{\rho_c/E_c}$ for a simply-supported Al/Al₂O₃ FGM square thick plate with a side crack ($h/b = 0.1$, $c_y/b = 0.5$, $d/a = 0.5$, $\alpha = 0^\circ$, $\hat{n} = 1$).

Mode No.	Crack functions \bar{N} (Eqs. (8))	Orthogonal polynomial solution size ($I \times J$)					
		5 × 5	7 × 7	9 × 9	10 × 10	11 × 11	12 × 12
1(S)	0	4.420	4.419	4.419	4.419	4.419	4.419
	5	4.124	4.124	4.122	4.122	4.122	4.122
	7	4.123	4.122	4.122	4.122	4.122	4.122
	9	4.122	4.122	4.122	4.122	4.122	4.122
	10	4.122	4.122	4.122	4.122	4.122	4.122
	11	4.122	4.122	4.122	4.122	4.122	4.122
	12	4.122	4.122	4.122	4.122	4.122	4.122
2(A)	0	10.62	10.59	10.59	10.59	10.59	10.59
	5	8.944	8.913	8.905	8.903	8.902	8.901
	7	8.908	8.884	8.874	8.872	8.871	8.870
	9	8.887	8.873	8.862	8.859	8.857	8.857
	10	8.880	8.868	8.859	8.856	8.854	8.853
	11	8.875	8.864	8.857	8.854	8.852	8.851
	12	8.871	8.861	8.855	8.853	8.851	8.850
3(S)	0	10.62	10.59	10.59	10.59	10.59	10.59
	5	10.25	10.25	10.25	10.25	10.25	10.25
	7	10.25	10.25	10.25	10.25	10.25	10.25
	9	10.25	10.25	10.25	10.25	10.25	10.25
	10	10.25	10.25	10.25	10.25	10.25	10.25
	11	10.25	10.25	10.25	10.25	10.25	10.25
	12	10.25	10.25	10.25	10.25	10.25	10.25
4(A)	0	16.20	16.20	16.20	16.20	16.20	16.20
	5	13.33	13.33	13.32	13.32	13.32	13.32
	7	13.32	13.32	13.32	13.32	13.32	13.32
	9	13.32	13.32	13.32	13.31	13.31	13.31
	10	13.32	13.32	13.31	13.31	13.31	13.31
	11	13.32	13.32	13.31	13.31	13.31	13.31
	12	13.32	13.31	13.31	13.31	13.31	13.31
5(A)	0	16.20	16.20	16.20	16.20	16.20	16.20
	5	13.50	13.50	13.50	13.50	13.50	13.50
	7	13.50	13.50	13.50	13.50	13.50	13.50
	9	13.50	13.50	13.50	13.49	13.49	13.49
	10	13.50	13.50	13.49	13.49	13.49	13.49
	11	13.50	13.50	13.49	13.49	13.49	13.49
	12	13.50	13.49	13.49	13.49	13.49	13.49

Table 5
Convergence of frequency parameters $\omega(b^2/h)\sqrt{\rho_c/E_c}$ for a simply-supported Al/Al₂O₃ FGM square thick plate with a side crack ($h/b = 0.1$, $c_y/b = 0.5$, $d/a = 0.9$, $\alpha = 0^\circ$, $\hat{n} = 1$).

Mode No.	Crack functions \bar{N} (Eqs. (8))	Orthogonal polynomial solution size ($I \times J$)					
		5 × 5	7 × 7	9 × 9	10 × 10	11 × 11	12 × 12
1(S)	0	4.420	4.419	4.419	4.419	4.419	4.419
	5	3.594	3.592	3.591	3.591	3.591	3.591
	7	3.592	3.591	3.590	3.590	3.590	3.590
	9	3.591	3.590	3.590	3.590	3.590	3.590
	10	3.591	3.590	3.590	3.590	3.590	3.590
	11	3.591	3.590	3.590	3.590	3.590	3.590
	12	3.591	3.590	3.590	3.590	3.590	3.590
2(A)	0	10.62	10.59	10.59	10.59	10.59	10.59
	5	4.593	4.555	4.549	4.547	4.547	4.546
	7	4.534	4.517	4.503	4.502	4.501	4.501
	9	4.506	4.497	4.488	4.483	4.482	4.481
	10	4.497	4.490	4.483	4.479	4.477	4.475
	11	4.490	4.484	4.479	4.476	4.474	4.472
	12	4.486	4.480	4.476	4.473	4.472	4.470
3(S)	0	10.62	10.59	10.59	10.59	10.59	10.59
	5	10.03	10.01	10.01	10.01	10.01	10.01
	7	10.01	10.01	10.00	10.00	10.00	10.00
	9	10.01	10.00	10.00	10.00	10.00	10.00
	10	10.01	10.00	10.00	10.00	10.00	10.00
	11	10.01	10.00	10.00	10.00	10.00	10.00
	12	10.01	10.00	10.00	10.00	10.00	10.00
4(A)	0	16.20	16.20	16.20	16.20	16.20	16.20
	5	11.78	11.67	11.65	11.64	11.64	11.64
	7	11.60	11.56	11.54	11.53	11.53	11.53
	9	11.54	11.52	11.50	11.49	11.49	11.49
	10	11.52	11.51	11.49	11.49	11.48	11.48
	11	11.51	11.50	11.49	11.48	11.48	11.47
	12	11.50	11.49	11.48	11.47	11.47	11.47
5(S)	0	16.20	16.20	16.20	16.20	16.20	16.20
	5	12.62	12.61	12.61	12.61	12.61	12.61
	7	12.61	12.61	12.61	12.61	12.61	12.61
	9	12.61	12.61	12.61	12.61	12.61	12.61
	10	12.61	12.61	12.61	12.61	12.61	12.61
	11	12.61	12.61	12.61	12.61	12.61	12.61
	12	12.61	12.61	12.61	12.61	12.61	12.61

It can be seen in Table 2 that increasing the number of orthogonal polynomial admissible functions ($I \times J$) from 5×5 to 11×11 employed in the present Ritz procedure leads to $\omega h \sqrt{\rho_m/E_m}$ solutions that converge to four significant figures monotonically as upper bounds on the exact $\omega h \sqrt{\rho_m/E_m}$ obtained from Reddy's analytical solution. Table 2 confirms the accuracy of the Ritz procedure developed in this work for the vibrations of FGM rectangular thick plates without a side crack. The results of Ferreira et al. [10] agree reasonably with the present analytical results. The Ferreira et al. [10] meshless local Petrov–Galerkin formulation does not yield $\omega h \sqrt{\rho_m/E_m}$ that monotonically converge to the exact Reddy solution, as the number of collocation points increases.

3.2. Side-cracked rectangular homogenous thin plate

To study the validity and accuracy of using the assumed hybrid series of orthogonal polynomials and crack functions, Table 3 summarizes a convergence study of non-dimensional frequency parameters $\omega(b^2/h)\sqrt{\rho_c/E_c}$ for a homogenous rectangular ($a/b = 2$) thin ($h/b = 0.01$) plate with a horizontal crack at $c_y/b = 0.5$ having length ratio $d/a = 0.5$. The homogenous material properties were established by setting $\hat{n} = 0$ in Eq. (10), and ceramic material properties (ρ_c , E_c , and ν_c) were assumed. It should be noted that for this thin plate the assumed in-plane displacement approximations

(u_0 and v_0) are negligibly coupled with the transverse displacement (w_0) and bending rotation components (ϕ_x and ϕ_y).

Table 3 presents the convergence of the first five non-dimensional frequency parameters $\omega(b^2/h)\sqrt{\rho_c/E_c}$ obtained using $4 \times 4, 5 \times 5, \dots, 9 \times 9$ orthogonal polynomial solution sizes in conjunction with increasing sets of crack functions with $\bar{N} = 0, 4, 5, 6$, and 7 in Eqs. (8) for each of the in-plane and transverse displacements and bending rotation components. The first five frequencies correspond to w_0 , ϕ_x and ϕ_y , because a very thin plate ($h/b = 0.01$) is under consideration. The plate is symmetrical about the horizontal line including the crack, so that the vibration modes are either symmetric or anti-symmetric about this line, and denoted by parenthesized (S) and (A) in the first column of Table 3, respectively. Table 3 also lists $\omega(b^2/h)\sqrt{\rho_c/E_c}$ of Stahl and Keer [47] and Huang and Leissa [16]. Stahl and Keer [47] used classical Kirchhoff thin plate theory and developed solutions using an accurate Fredholm integration approach. Similarly, Huang and Leissa [16] employed classical Kirchhoff thin plate theory in conjunction with the Ritz method. The convergence study reveals that polynomial functions alone do not yield the correct convergent solutions. Adding the crack functions into the admissible functions significantly accelerates the upper bound convergence of $\omega(b^2/h)\sqrt{\rho_c/E_c}$ to the accurate values, which agree very closely with the $\omega(b^2/h)\sqrt{\rho_c/E_c}$ of Stahl and Keer [47] and Huang and

Table 6

Frequency parameters $\omega(b^2/h)\sqrt{\rho_c/E_c}$ for simply supported square Al/Al₂O₃ FGM plates with side cracks ($h/b = 0.1$).

\hat{n}	α (degrees)	c_y/b	d/a	Mode						
				1	2	3	4	5		
0	0	0.5	0	5.769	13.76	13.76	19.48*	19.48*		
				0.1	5.768	13.74	13.76	19.25*	19.48*	
				0.2	5.750	13.68	13.70	18.56*	19.48*	
				0.3	5.690	13.52	13.56	17.63*	19.48*	
				0.4	5.565	12.92	13.40	16.78*	18.67	
				0.5	5.379	11.45	13.32	16.18*	17.32	
	0	0.75	0.1	5.759	13.75	13.76	19.12*	19.48*		
				0.2	5.738	13.65	13.74	18.11*	19.48*	
				0.3	5.689	13.32	13.70	16.80*	19.48*	
				0.4	5.591	12.75	13.53	15.63*	19.46*	
				0.5	5.418	12.09	13.05	14.73*	17.25	
				0.6	5.167	11.31	12.21	14.05*	15.27	
	45	0.75	0.1	5.757	13.73	13.76	19.20*	19.48*		
				0.2	5.721	13.58	13.74	18.38*	19.48*	
				0.3	5.650	13.24	13.67	17.19*	19.47*	
				0.4	5.533	12.78	13.40	15.91*	19.44*	
				0.5	5.371	12.21	12.71	14.75*	17.69	
				0.6	5.178	10.77	12.31	13.75*	16.13	
	0.2	0	0.5	0	5.363	12.82	12.82	18.56	18.56	
					0.1	5.362	12.80	12.82	18.34	18.56
					0.2	5.346	12.75	12.76	17.68	18.56
					0.3	5.290	12.60	12.63	16.80	18.56
					0.4	5.174	12.05	12.48	15.98	17.43
					0.5	5.001	10.68	12.41	15.42	16.15
0		0.75	0.1	5.354	12.81	12.82	18.22	18.56		
				0.2	5.334	12.71	12.80	17.25	18.56	
				0.3	5.291	12.41	12.76	16.01	18.56	
				0.4	5.200	11.88	12.61	14.89	18.53	
				0.5	5.039	11.26	12.16	14.03	16.11	
				0.6	4.808	10.54	11.38	13.39	14.26	
45		0.75	0.1	5.352	12.79	12.82	18.29	18.56		
				0.2	5.319	12.65	12.80	17.51	18.56	
				0.3	5.253	12.34	12.73	16.38	18.55	
				0.4	5.145	11.91	12.49	15.16	18.45	
				0.5	4.995	11.37	11.85	14.05	16.50	
				0.6	4.816	10.05	11.47	13.10	15.04	
1		0	0.5	0	4.419	10.59	10.59	16.20	16.20	
					0.1	4.418	10.57	10.59	16.00	16.20
					0.2	4.405	10.53	10.54	15.43	16.16
						(4.393)	(10.52)	(10.54)	(15.48)	(16.17)
					0.3	4.359	10.41	10.43	14.66	15.70
					0.4	4.264	9.973	10.31	13.95	14.44
	0	0.75	0.1	4.412	10.58	10.59	15.90	16.20		
				0.2	4.396	10.50	10.57	15.05	16.15	
				0.3	4.361	10.25	10.54	13.97	15.80	
				0.4	4.287	9.807	10.42	13.00	15.34	
				0.5	4.156	9.295	10.05	12.24	13.37	
				0.6	3.965	8.701	9.402	11.64	11.85	
	45	0.75	0.1	4.410	10.57	10.59	15.97	16.20		
				0.2	4.384	10.45	10.58	15.28	16.20	
				0.3	4.329	10.19	10.52	14.29	16.01	
				0.4	4.242	9.836	10.32	13.23	15.30	
				0.5	4.120	9.396	9.811	12.26	13.69	
				0.6	3.972	8.314	9.482	11.44	12.44	
	5	0	0.5	0	3.768	8.909	8.909	12.64	12.64	
					0.1	3.767	8.889	8.905	12.48	12.64
					0.2	3.756	8.851	8.867	12.04	12.64
					0.3	3.716	8.738	8.774	11.44	12.64
					0.4	3.633	8.336	8.672	10.88	11.99
					0.5	3.511	7.379	8.621	10.49	11.17
0.6	3.368	6.197	8.616	10.28	10.96					

Table 6 (continued)

\hat{n}	α (degrees)	c_y/b	d/a	Mode					
				1	2	3	4	5	
0	0	0.75	0.1	3.761	8.897	8.906	12.41	12.64	
				0.2	3.746	8.831	8.895	11.75	12.64
				0.3	3.714	8.618	8.865	10.90	12.63
				0.4	3.648	8.250	8.755	10.14	12.61
				0.5	3.534	7.822	8.435	9.554	11.04
				0.6	3.370	7.306	7.894	9.112	9.834
	45	0.75	0.1	3.760	8.887	8.907	12.45	12.64	
				0.2	3.736	8.787	8.894	11.92	12.64
				0.3	3.688	8.564	8.843	11.15	12.63
				0.4	3.611	8.262	8.661	10.32	12.53
				0.5	3.503	7.884	8.207	9.572	11.32
				0.6	3.376	6.947	7.956	8.930	10.37
10	0	0.5	0	3.637	8.563	8.563	11.53	11.53	
				0.1	3.636	8.544	8.559	11.38	11.53
				0.2	3.625	8.506	8.523	10.98	11.53
				0.3	3.586	8.392	8.434	10.43	11.53
				0.4	3.506	7.995	8.337	9.924	11.47
				0.5	3.388	7.062	8.289	9.569	10.71
	0	0.75	0.1	3.630	8.551	8.560	11.31	11.53	
				0.2	3.615	8.488	8.549	10.71	11.52
				0.3	3.583	8.284	8.519	9.941	11.52
				0.4	3.519	7.932	8.412	9.247	11.51
				0.5	3.407	7.524	8.100	8.715	10.55
				0.6	3.248	7.024	7.583	8.315	9.415
45	0.75	0.1	3.629	8.542	8.561	11.36	11.53		
			0.2	3.605	8.443	8.548	10.87	11.52	
			0.3	3.558	8.230	8.497	10.17	11.52	
			0.4	3.483	7.940	8.316	9.413	11.49	
			0.5	3.379	7.576	7.872	8.728	10.83	
			0.6	3.255	6.659	7.642	8.143	9.939	

* :in-plane mode; (): 3-D elasticity-based FEM solutions.

Leissa [16]. In Table 3 the $\omega(b^2/h)\sqrt{\rho_c/E_c}$ obtained using an $I \times J + \bar{N} = 9 \times 9 + 7$ solution are accurate to at least three significant figures and are slightly lower upper bounds on the exact solution than the $\omega(b^2/h)\sqrt{\rho_c/E_c}$ previously reported in Stahl and Keer [47] and Huang and Leissa [16]. Because Stahl and Keer [47] and Huang and Leissa [16] employed the classical plate theory, their analysis underestimates the flexural displacements and overestimates the flexural vibrations of a cracked plate. Classical Kirchhoff thin-plate theory overestimates the flexural rigidity of a cracked plate by neglecting its transverse shear flexibility.

3.3. Side-cracked square FGM thick plates

Tables 4 and 5 present the convergence studies of the first five non-dimensional frequency parameters, $\omega(b^2/h)\sqrt{\rho_c/E_c}$, for a thick ($h/a = 0.1$) square plate having a horizontal side crack at $c_y/b = 0.5$ with $d/a = 0.5$ and $d/a = 0.9$, respectively. The plate comprises aluminum (Al) and alumina (Al₂O₃), and the distribution of material properties along the thickness direction is described by Eq. (10) with $\hat{n} = 1$. The numerical results were obtained using $5 \times 5, 7 \times 7, 9 \times 9, 10 \times 10, 11 \times 11$, and 12×12 orthogonal polynomial solution sizes in conjunction with sets of crack functions with $\bar{N} = 0, 5, 7, 9, 10, 11$, and 12 in Eqs. (8) for each of the in-plane and transverse bending displacements and rotation components. Again, the use of orthogonal polynomials alone does not yield fully converged $\omega(b^2/h)\sqrt{\rho_c/E_c}$ solutions. In Table 4, adding sets of crack functions with $\bar{N} = 5$ to the 5×5 polynomial solution size yields $\omega(b^2/h)\sqrt{\rho_c/E_c}$ that converge to the accurate values to three significant figures, except for the second mode, while sets of

Table 7
Frequency parameters $\omega(b^2/h)\sqrt{\rho_c/E_c}$ for cantilevered square Al/ZrO₂ FGM plates with horizontal side cracks ($h/b = 0.1$, $c_y/b = 0.5$).

\hat{n}	d/a	Mode				
		1	2	3	4	5
0	0.	1.038	2.441	6.086	6.583*	7.721
	0.1	1.038	2.424	6.062	6.583*	7.429
	0.2	1.038	2.353	5.792	6.571*	6.881
	0.3	1.038	2.208	5.709	6.442	6.525*
	0.4	1.038	1.990	5.255	5.838	6.266*
	0.5	1.038	1.733	4.810	5.218	6.185*
	0.6	1.038	1.487	4.456	4.850	5.837*
0.2	0.	1.008	2.374	5.919	6.509	7.509
	0.1	1.008	2.356	5.894	6.508	7.224
	0.2	1.008	2.287	5.807	6.497	6.692
	0.3	1.008	2.146	5.552	6.265	6.451
	0.4	1.008	1.934	5.112	5.682	6.093
	0.5	1.008	1.684	4.679	5.078	6.025
	0.6	1.007	1.445	4.336	4.720	5.770
1	0.	0.9553	2.250	5.614	6.300	7.122
	0.1	0.9553	2.235	5.592	6.300	6.854
	0.2	0.9553	2.169	5.509	6.289	6.350
	0.3	0.9551	2.035	5.268	5.945	6.232
	0.4	0.9550	1.835	4.852	5.393	5.781
	0.5	0.9549	1.597	4.441	4.820	5.716
	0.6	0.9547	1.370	4.115	4.481	5.587
5	0.	0.9748	2.281	5.675	5.947	7.203
	0.1	0.9748	2.265	5.652	5.947	6.926
	0.2	0.9747	2.199	5.568	5.936	6.412
	0.3	0.9745	2.063	5.320	5.892	6.002
	0.4	0.9744	1.861	4.894	5.424	5.794
	0.5	0.9743	1.621	4.476	4.850	5.590
	0.6	0.9741	1.392	4.145	4.508	5.275
10	0.	0.9727	2.274	5.658	5.829	7.182
	0.1	0.9727	2.259	5.636	5.829	6.906
	0.2	0.9726	2.193	5.551	5.818	6.392
	0.3	0.9724	2.058	5.303	5.776	5.984
	0.4	0.9723	1.856	4.878	5.406	5.678
	0.5	0.9722	1.617	4.462	4.834	5.478
	0.6	0.9720	1.388	4.132	4.493	5.169

Table 8
Frequency parameters $\omega(b^2/h)\sqrt{\rho_c/E_c}$ for cantilevered rectangular Al/ZrO₂ FGM plates with vertical side cracks ($h/b = 0.1$, $c_x/a = 0.5$).

a/b	\hat{n}	d/b	Mode				
			1	2	3	4	5
1	0	0.1	1.033	2.417	5.957	6.498*	7.676
		0.2	1.017	2.322	5.655	6.197*	7.473
		0.3	0.9901	2.156	5.264	5.617*	7.043
		0.4	0.9477	1.946	4.788*	4.862	6.485
		0.5	0.8853	1.729	3.848*	4.485	5.979
		0.6	0.8012	1.542	2.922*	4.137	5.607
	0.2	0.1	1.003	2.349	5.792	6.424	7.463
		0.2	0.9876	2.257	5.499	6.126	7.266
		0.3	0.9613	2.095	5.119	5.553	6.848
		0.4	0.9203	1.891	4.727	4.735	6.308
		0.5	0.8599	1.681	3.804	4.361	5.816
		0.6	0.7785	1.498	2.888	4.024	5.454
	1	0.1	0.9501	2.228	5.495	6.219	7.080
		0.2	0.9361	2.141	5.218	5.931	6.893
		0.3	0.9112	1.987	4.857	5.376	6.498
		0.4	0.8724	1.793	4.486	4.584	5.986
		0.5	0.8154	1.594	3.682	4.139	5.520
		0.6	0.7383	1.421	2.796	3.818	5.176
	5	0.1	0.9693	2.258	5.554	5.87	7.162
		0.2	0.9545	2.170	5.272	5.598	6.972
		0.3	0.9285	2.014	4.905	5.074	6.566
		0.4	0.8882	1.818	4.325	4.532	6.041
		0.5	0.8290	1.617	3.476	4.180	5.566
		0.6	0.7495	1.442	2.639	3.856	5.219
	10	0.1	0.9672	2.252	5.537	5.754	7.141
		0.2	0.9524	2.164	5.255	5.487	6.951
		0.3	0.9264	2.009	4.890	4.974	6.546
		0.4	0.8861	1.813	4.239	4.518	6.022
		0.5	0.8269	1.612	3.407	4.167	5.549
		0.6	0.7475	1.438	2.587	3.844	5.202
2	0	0	0.2590	1.074	1.596	2.173*	3.464
		0.1	0.2583	1.069	1.579	2.152*	3.444
		0.2	0.2566	1.049	1.541	2.090*	3.390
		0.3	0.2537	1.013	1.486	1.982*	3.309
		0.4	0.2495	0.9640	1.421	1.821*	3.172
		0.5	0.2437	0.9017	1.348	1.602*	2.932
	0.2	0	0.2514	1.044	1.550	2.149	3.370
		0.1	0.2507	1.038	1.534	2.128	3.347
		0.2	0.2490	1.019	1.496	2.066	3.297
		0.3	0.2462	0.9843	1.443	1.960	3.216
		0.4	0.2422	0.9367	1.380	1.801	3.084
		0.5	0.2365	0.8761	1.309	1.584	2.851
	1	0	0.2382	0.9892	1.469	2.080	3.192
		0.1	0.2376	0.9844	1.454	2.060	3.175
		0.2	0.236	0.9660	1.418	2.000	3.127
		0.3	0.2333	0.9333	1.368	1.897	3.050
		0.4	0.2295	0.8882	1.308	1.743	2.926
		0.5	0.2242	0.8307	1.241	1.533	2.705
	5	0	0.2169	0.7636	1.171	1.269	2.434
		0.1	0.2434	1.005	1.497	1.963	3.237
		0.2	0.2427	1.000	1.481	1.944	3.218
		0.3	0.2411	0.9816	1.445	1.888	3.170
		0.4	0.2383	0.9485	1.393	1.791	3.091
		0.5	0.2343	0.9025	1.331	1.645	2.963
	10	0	0.2288	0.8440	1.263	1.447	2.736
		0.1	0.2213	0.7752	1.191	1.198	2.460
		0	0.2422	1.003	1.494	1.924	3.228
		0.1	0.2422	0.9977	1.478	1.906	3.209
		0.2	0.2406	0.9792	1.441	1.851	3.161
		0.3	0.2378	0.9461	1.390	1.755	3.083
2	0	0.2338	0.9002	1.328	1.613	2.954	
	0.1	0.2283	0.8418	1.260	1.419	2.728	
	0.2	0.2208	0.7732	1.174	1.188	2.453	

crack functions with $\bar{N} = 9$ with 9×9 polynomials are needed for the case with $d/a = 0.9$ in Table 5. Increasing the orthogonal polynomial solution sizes and the crack functions further improves the accuracy of $\omega(b^2/h)\sqrt{\rho_c/E_c}$ solutions.

4. Frequency parameters and mode shapes

After the correctness of the proposed approach was verified by performing the convergence studies, further extensive convergence studies were carried out to determine the least upper bounds on the first five non-dimensional frequency parameters $\omega(b^2/h)\sqrt{\rho_c/E_c}$ for simply-supported and cantilevered rectangular plates with side cracks in various configurations. The plates examined are made of aluminum and alumina (Al/Al₂O₃) or aluminum and zirconia (Al/ZrO₂). The variations of the material properties are assumed to follow Eq. (10) or the Mori-Tanaka scheme with various \hat{n} . The effects of crack configurations and material distributions on the vibration frequencies are comprehensively investigated. In Tables 5–7, $\omega(b^2/h)\sqrt{\rho_c/E_c}$ for plates with crack length d/a (or d/b) = 0.1 or 0.2 were obtained using $I \times J + \bar{N} = 9 \times 9 + 5$ solutions yielding a total of 605 degrees of freedom in Eq. (9); $\omega(b^2/h)\sqrt{\rho_c/E_c}$ for d/a (or d/b) = 0.5 and 0.6 were obtained using $I \times J + \bar{N} = 10 \times 10 + 10$ solutions resulting in a total of 1150 degrees of freedom. The $\omega(b^2/h)\sqrt{\rho_c/E_c}$ for d/a (or d/b) = 0.3 and 0.4 were obtained using $I \times J + \bar{N} = 9 \times 9 + 8$ solutions yielding a total of 845 degrees of freedom. The $\omega(b^2/h)\sqrt{\rho_c/E_c}$ for intact plates were obtained using $I \times J + \bar{N} = 11 \times 11 + 0$ solutions. Extensive convergence studies, not presented here, indicate that

most of the frequency parameters $\omega(b^2/h)\sqrt{\rho_c/E_c}$ converged to at least three significant figures.

Table 6 presents the first five non-dimensional frequency parameters $\omega(b^2/h)\sqrt{\rho_c/E_c}$ for simply-supported square Al/Al₂O₃ FGM thick plates ($h/b = 0.1$) with side cracks of various lengths ($d/a = 0.1, 0.2, \dots, 0.6$), orientations ($\alpha = 0^\circ$ and 45°), and locations ($c_y/b = 0.5$ and 0.75). The variation of material properties in the thickness direction is given by Eq. (10). Fig. 2 plots the variations in Young's modulus and density in the thickness direction for $\hat{n} = 0.2, 1, 5,$ and 10 . In the results for homogeneous plates ($\hat{n} = 0$), the superscript "*" denotes frequencies of in-plane modes, which occur at the fourth or fifth mode. When the fifth mode is an in-plane mode, its frequency does not significantly change with the crack length.

As expected, increasing the crack length reduces the frequency of each mode because it reduces the stiffness of the plate. Nevertheless, unlike those of the other modes summarized in Table 6, the $\omega(b^2/h)\sqrt{\rho_c/E_c}$ of the third modes for plates with horizontal cracks at $c_y/b = 0.5$ do not vary substantially with the crack length, and the change in $\omega(b^2/h)\sqrt{\rho_c/E_c}$ is less than 3.5% as d/a increases from 0 to 0.6. Moving the crack from $c_y/b = 0.5$ to $c_y/b = 0.75$ or changing the crack orientation from $\alpha = 0^\circ$ to $\alpha = 45^\circ$ may reduce or increase $\omega(b^2/h)\sqrt{\rho_c/E_c}$, depending on the mode and crack length. A small crack $d/a = 0.1$ in various locations and orientations causes $\omega(b^2/h)\sqrt{\rho_c/E_c}$ to differ slightly from those for intact plates, with a difference of less than 2%. A small crack $d/a = 0.1$ has a greater effect on the fourth mode than on any of the other of the first five modes, and the least effect on the fifth mode. Increasing the volume fraction exponent \hat{n} reduces the ceramic component of the plates. Naturally, the $\omega(b^2/h)\sqrt{\rho_c/E_c}$ decreases as \hat{n} increases,

because increasing \hat{n} reduces the stiffness more than it does the mass of Al/Al₂O₃ FGM plates.

In Table 6, parenthesized numerical results of $\omega(b^2/h)\sqrt{\rho_c/E_c}$ for the cases of $d/a = 0.2$ and 0.5 , $\alpha = 0^\circ$, $c_y/b = 0.5$, and $\hat{n} = 1$ were calculated by the ABAQUS finite element package, in which twenty-node isoparametric quadratic brick elements (C3D20R) were used. These results were obtained based on 3-D elasticity theory and using 40 elements in each of x, y and z directions (resulting in 130791 nodes). Because the material properties linearly vary in z direction (thickness direction), material properties in an element were set equal to the average material properties in the element. Comparing the present results with the finite element results, one finds less than 0.4% differences.

Tables 7 and 8 list the first five non-dimensional frequency parameters $\omega(b^2/h)\sqrt{\rho_c/E_c}$ for cantilevered rectangular Al/ZrO₂ FGM thick plates ($h/b = 0.1$) with side cracks of different crack lengths (d/a (or d/b) = 0.1, 0.2, ..., 0.6). The plates are clamped along $x = 0$. Table 7 considers only square plates with horizontal side cracks at $c_y/b = 0.5$, while Table 8 considers rectangular plates ($a/b = 1$ and 2) with vertical side cracks at $c_x/a = 0.5$ (Fig. 1b). Superscript "*" refers to the frequencies of in-plane modes for homogeneous plates. The material properties in the direction of thickness are estimated using the power law given in Eq. (10). Fig.3 plots the variations in Young's modulus and density in the thickness direction for $\hat{n} = 0.2, 1, 5,$ and 10 .

Again, it is observed that increasing of crack length reduces $\omega(b^2/h)\sqrt{\rho_c/E_c}$. Table 7 shows that increasing the crack length d/a from 0 to 0.6 does not significantly reduce $\omega(b^2/h)\sqrt{\rho_c/E_c}$ of

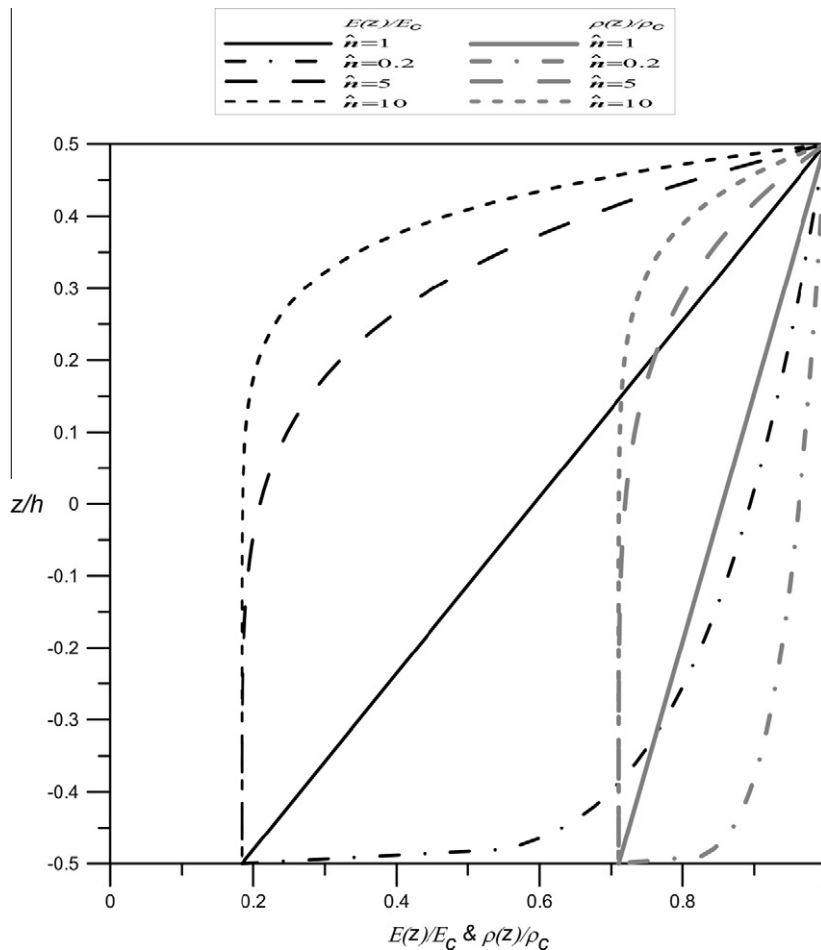


Fig. 2. Variations of $E(z)$ and $\rho(z)$ for Al/Al₂O₃ through the thickness according to Eq. (10).

Table 9
Effects of material models on frequency parameters $\omega(b^2/h)\sqrt{\rho_c/E_c}$ of cantilevered square Al/Al₂O₃ FGM plates having horizontal side cracks with $c_y/b = 0.5$ and $d/a = 0.4$.

h/b	\hat{n}	Material model	Model				
			1	2	3	4	5
0.05	0.2	Eq. (10)	1.016	1.994	5.408	6.030	6.352
		Mori–Tanaka	0.9925	1.951	5.294	5.900	6.208
	1	Eq. (10)	0.7991	1.571	4.263	4.754	5.003
		Mori–Tanaka	0.7569	1.492	4.049	4.509	4.736
	5	Eq. (10)	0.6883	1.348	3.643	4.062	4.290
		Mori–Tanaka	0.6721	1.317	3.561	3.968	4.187
	10	Eq. (10)	0.6664	1.303	3.519	3.923	4.148
		Mori–Tanaka	0.6472	1.268	3.427	3.818	4.030
0.2	0.2	Eq. (10)	0.9821	1.795	3.168	4.450	4.583
		Mori–Tanaka	0.9601	1.757	3.110	4.353	4.502
	1	Eq. (10)	0.7743	1.421	2.659	3.464	3.864
		Mori–Tanaka	0.7330	1.347	2.498	3.261	3.653
	5	Eq. (10)	0.6603	1.191	2.071	2.780	3.155
		Mori–Tanaka	0.6443	1.162	1.976	2.705	3.012
	10	Eq. (10)	0.6373	1.144	1.892	2.634	2.913
		Mori–Tanaka	0.6197	1.116	1.832	2.578	2.810

the first mode. Of the first five modes in Table 8, the crack length most reduces $\omega(b^2/h)\sqrt{\rho_c/E_c}$ of the third mode for square plates and the fourth mode of plates with $a/b = 2$. A small horizontal crack ($d/a = 0.1$), as presented in Table 7, reduces $\omega(b^2/h)\sqrt{\rho_c/E_c}$ of the first four modes, and especially the first mode, for cracked plates

by less than 0.7%. Table 8 reveals that a small vertical crack ($d/b = 0.1$) reduces the first five non-dimensional frequency parameters by less than 2.2% from those for an intact plate. In contrast to the findings in Table 6, increasing the volume fraction exponent \hat{n} does not necessarily reduce $\omega(b^2/h)\sqrt{\rho_c/E_c}$. This trend was also observed elsewhere [12] in an investigation of the vibrations of intact square FGM plates. The effects of \hat{n} on $\omega(b^2/h)\sqrt{\rho_c/E_c}$ of Al/ZrO₂ FGM plates differ markedly from those of Al/Al₂O₃ FGM plates, primarily because Al/Al₂O₃ FGM has a much larger $\frac{\rho_m/\rho_c}{E_m/E_c}$ than Al/ZrO₂ FGM.

To demonstrate the effects of different models of describing the material properties in the thickness direction (Eq. (10) and Mori–Tanaka scheme) on the natural frequencies of plates, Table 9 displays the first five non-dimensional frequency parameters $\omega(b^2/h)\sqrt{\rho_c/E_c}$ for cantilevered square Al/Al₂O₃ FGM plates with horizontal side cracks with $c_y/b = 0.5$ and $d/a = 0.4$. Two thicknesses of the plate ($h/b = 0.05$ and 0.2) and four values of \hat{n} ($=0.2, 1, 5,$ and 10) are considered. Notably, the Reddy’s shear deformable theory is very suitable for thin ($h/b = 0.05$) to moderately thick plates ($h/b = 0.1$), but may not be accurate enough for thick plates with $h/b = 0.2$. Nevertheless, the results for $h/b = 0.2$ shown in Table 9 serve for the purpose of investigating the effects of different material models on vibration frequencies. For the case of very thick plates, Kant’s theory [34] is more accurate, which is the focus of continuing research. Eq. (10) and the Mori–Tanaka scheme yield the same distribution of mass density in the thickness direction, while the former yields larger values of $E(z)$ than the latter (Fig. 4). Consequently, the Mori–Tanaka scheme, used to describe

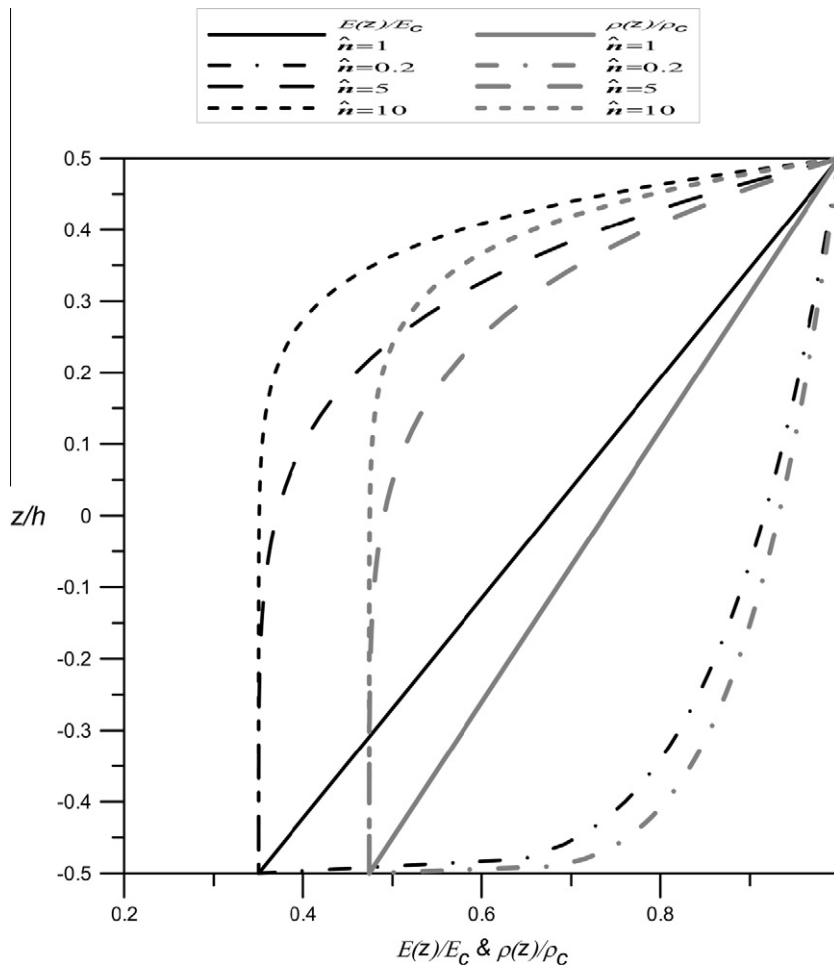


Fig. 3. Variations of $E(z)$ and $\rho(z)$ for all Al/ZrO₂ through the thickness according to Eq. (10).

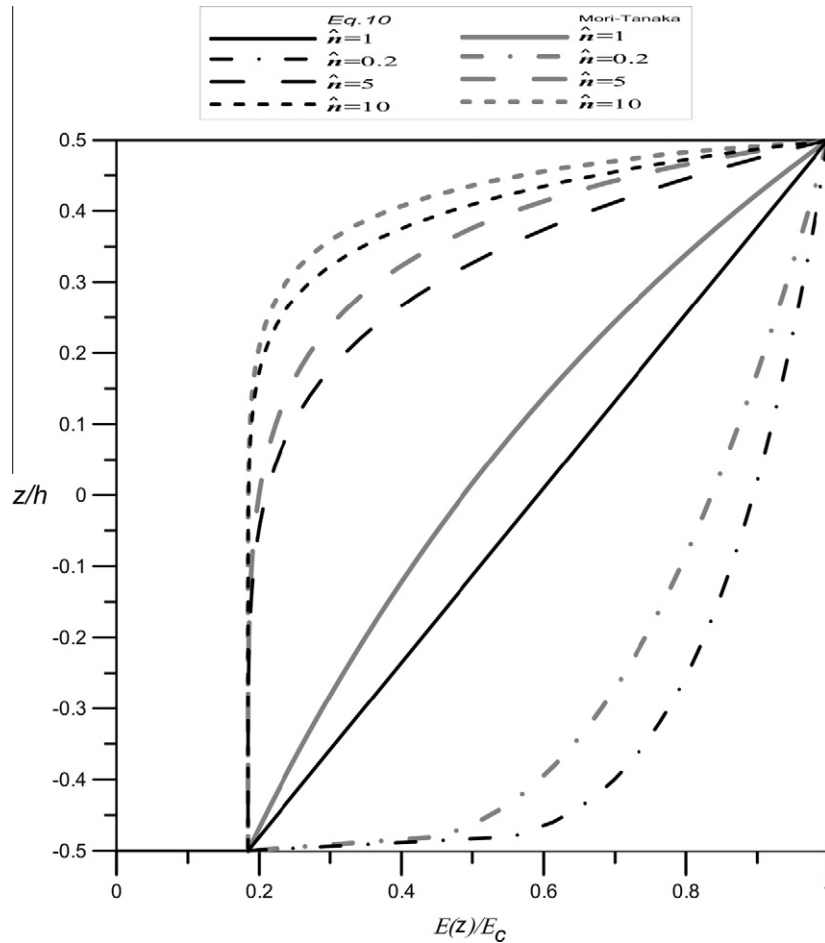


Fig. 4. Variations of $E(z)$ for Al/Al₂O₃ through the thickness according to Eq. (10) and the Mori–Tanaka scheme.

the variations of material properties in the thickness direction, yields smaller $\omega(b^2/h)\sqrt{\rho_c/E_c}$ than Eq. (10) with the largest difference of around 6% in the case of $\hat{n} = 1$ and $h/b = 0.2$. Generally speaking, the differences in $\omega(b^2/h)\sqrt{\rho_c/E_c}$ caused by these two material models are not significantly affected by the thickness of plate.

Depicted in Figs. 5–7 are nodal patterns and $\omega(b^2/h)\sqrt{\rho_c/E_c}$ for simply-supported and cantilevered moderately thick FGM plates ($h/b = 0.1$). The influence of volume fraction (\hat{n}), crack length ratios (d/a or d/b), and crack positions (c_x/a or c_y/b) on the nodal patterns are studied. No published vibration nodal patterns using higher-order shear deformable plate theories for cracked homogeneous and FGM simply-supported and cantilevered thick plates are known to exist.

For cracked thick FGM plates shear deformation and rotary inertia effects are significant in the lower predominately flexural modes and substantially in the higher ones, while large elastic warping stresses considerably increase in the predominately torsional modes. Vibratory stresses become unbounded near the crack tip, showing a well-known fracture mechanics fact that the order of 3-D components of stresses are $\sigma_{ij} \sim O(r^{-1/2})$, as r approaches zero (see Fig. 1). Nonetheless, these unbounded stresses oftentimes lead to theoretical prediction errors in the lower modes as well as some of the higher modes of cracked thick FGM plates. In the present thick plate formulation, complicating effects, such as shear deformation, rotary inertia, and elastic warping stresses at the hinged and clamped edges of the nodal patterns depicted in Figs. 5–7 are inherent.

All possible coupled shear deformable vibratory displacement patterns falling within the first five modes are depicted in Figs. 5–7. For an intact homogeneous thick plate, longitudinal flexure, sideways flexure, longitudinal extension, and torsional modes (even dilatational modes) are each uncoupled, forming four distinct symmetry classes of vibratory motion. For cracked FGM thick plates, depending on the volume fraction (\hat{n}), crack length ratios (d/a or d/b), crack positions (c_x/a or c_y/b), and crack inclination angles (α), distinct symmetry classes of modes may be possible with coupled longitudinal flexure and torsional modes classified into one symmetry class, and coupled sideways flexure and longitudinal extensional modes classified into a second symmetry class. Generally speaking, for $\hat{n} \neq 0$, d/a (or d/b) $\neq 0$, c_x/a (or c_y/b) $\neq 0$, and $\alpha \neq 0^\circ$, all possible modes are inseparably coupled with no identifiable symmetry classes present.

The dynamic stress field near the crack tip within an FGM thick plate may be classified as three basic dynamic responses each associated with a local mode of crack deformation. First, a crack opening mode in FGM thick plate vibration is associated with local displacement in which the crack surfaces move directly apart; second, a crack shearing or edge-sliding mode in FGM thick plate vibration is characterized by deformations in which the crack surfaces slide over one another perpendicular to the tip of the crack; third, a crack tearing mode in FGM thick plate vibration finds the crack surfaces sliding with respect to one another parallel to the tip of the crack. Crack opening and crack shearing or edge-sliding in FGM thick plate vibration can be modeled as two-dimensional plane-extension theory of elasticity, classified as symmetric (crack

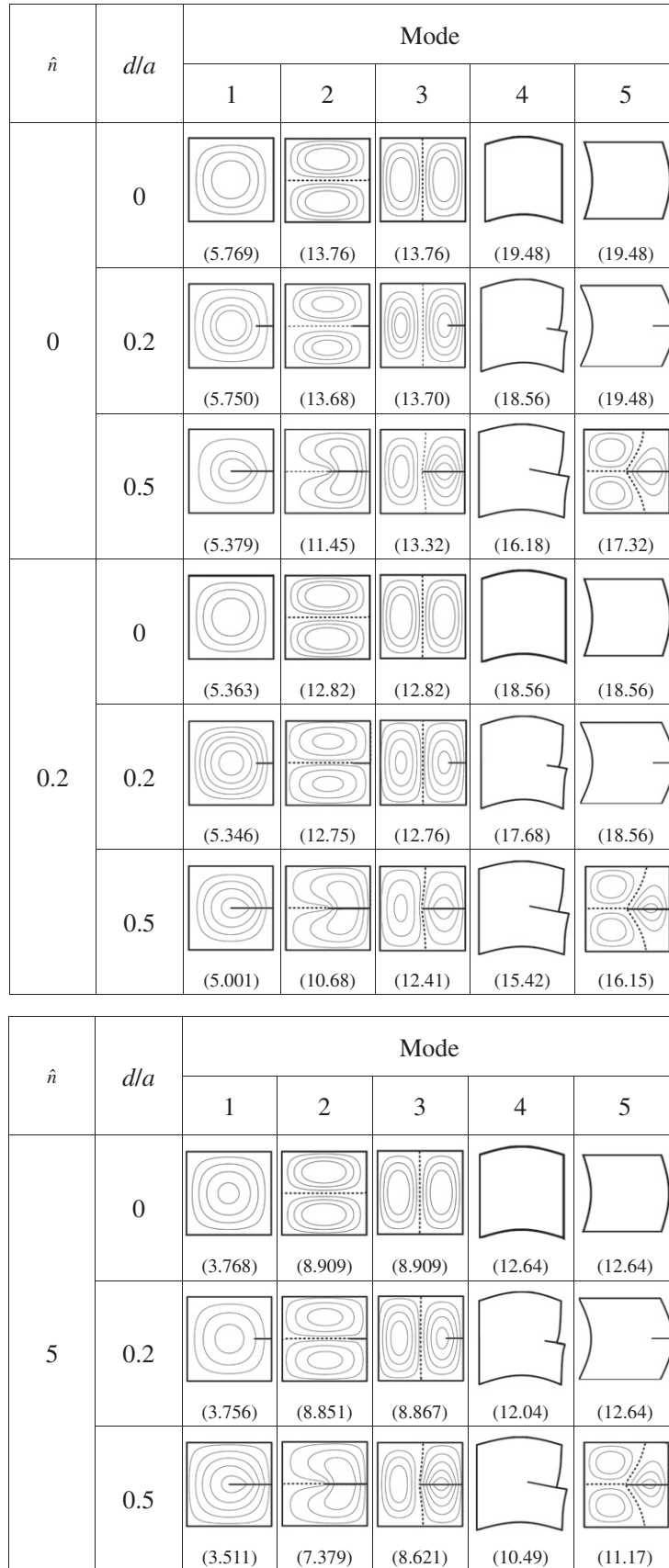


Fig. 5. Nodal patterns and $\omega(b^2/h)\sqrt{\rho_c/E_c}$ for simply-supported square moderately thick cracked Al/Al₂O₃ FGM plate ($\hat{n} = 0, 0.2, 5, d/a = 0, 0.2, 0.5, h/b = 0.1, c_y/b = 0.5, \alpha = 0^\circ$).

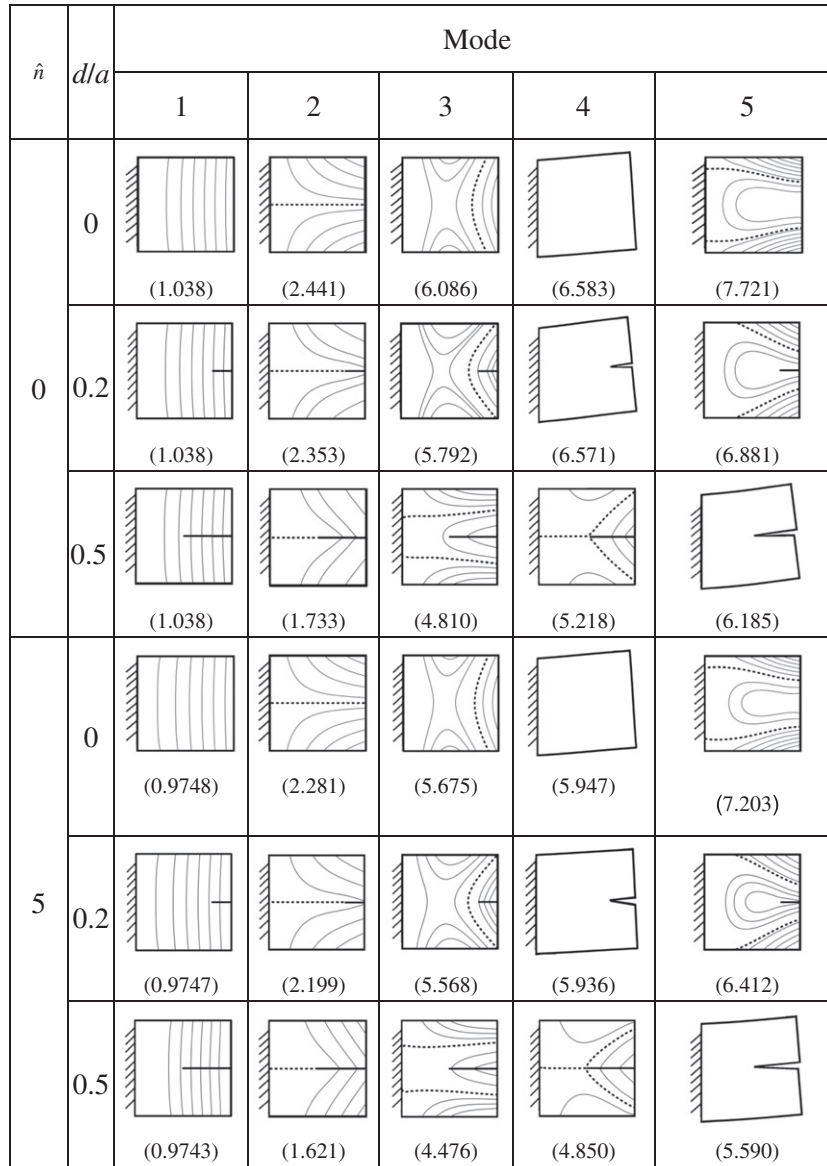


Fig. 6. Nodal patterns and $\omega(b^2/h)\sqrt{\rho_c/E_c}$ for cantilevered square moderately thick cracked Al/ZrO₂ FGM plate ($\hat{n} = 0, 5, d/a = 0, 0.2, 0.5, h/b = 0.1, c_y/b = 0.5, \alpha = 0^\circ$).

opening) and skew-symmetry (crack shearing/sliding) with respect to the tip of the crack. Crack tearing in FGM thick plate vibration may be modeled as two-dimensional pure shear (or torsion). Well-known superposition of crack opening, shearing or sliding, and tearing modes or “mixed mode” cracking in FGM thick plate vibration is sufficient to describe the most general three-dimensional dynamic aspects of local crack-edge deformation and stress fields in cracked thick plates.

The nodal patterns depicted in Figs. 5–7 show only the deformations on the mid-plane. Figs. 5–7 illustrate the first five vibration mode shapes for some of the square plates considered in Tables 6–8. Blank nodal patterns (i.e., containing no contours and nodal lines) indicate in-plane displacement dominated modes, showing the displacements of u_0 and v_0 along the edges, including predominately crack opening, crack shearing and sliding or crack tearing in some cases. For the out-of-plane flexural modes, the nodal patterns depict the primarily out-of-plane displacements, showing nodal lines represented by dash lines. Generally speaking, the nodal patterns are not significantly affected by the values of volume fraction (\hat{n}).

Depicted in Fig. 5 are nodal patterns and $\omega(b^2/h)\sqrt{\rho_c/E_c}$ for simply-supported Al/Al₂O₃ FGM square moderately thick plates ($\hat{n} = 0, 0.2, 5, d/a = 0, 0.2, 0.5, h/b = 0.1, c_y/b = 0.5, \alpha = 0^\circ$), which show first predominately longitudinal flexure (Mode 1), followed by a pair of second predominately longitudinal flexure showing single nodal lines each transverse to the hinged plate edges (Modes 2 and 3), and finally a pair of longitudinal extension modes, showing in-plane curvatures of parallel hinged plate edges (Modes 4 and 5 for $d/a = 0, 0.2$). Shown in Fig. 6 are nodal patterns and $\omega(b^2/h)\sqrt{\rho_c/E_c}$ for cantilevered cracked Al/ZrO₂ FGM square moderately thick plates ($\hat{n} = 0, 5, d/a = 0, 0.2, 0.5, h/b = 0.1, c_y/b = 0.5, \alpha = 0^\circ$), which show first predominately longitudinal flexure (Mode 1), followed by predominately torsion having a single nodal line spanning between the clamped and free ends (Mode 2), then second predominately longitudinal flexure showing single nodal lines transverse to the free plate edges (Modes 3 for $d/a = 0, 0.2$), next longitudinal extension showing in-plane curvatures of parallel free plate edges (Modes 4 for $d/a = 0, 0.2$), and finally, predominately chordwise flexure showing a pair of nodal lines spanning between the clamped and free ends (Modes 5 for $d/a = 0$ and 0.2). For thick

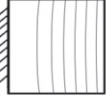
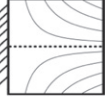
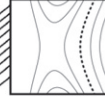

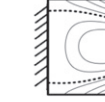
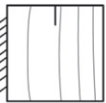
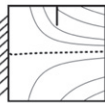
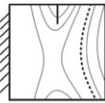

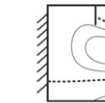
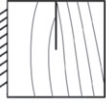
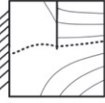

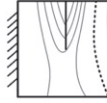
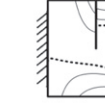
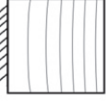
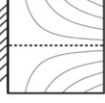


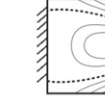
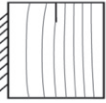
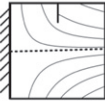
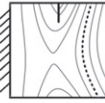

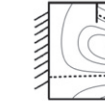
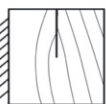
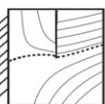

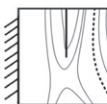
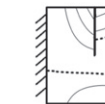
\hat{n}	d/b	Mode				
		1	2	3	4	5
0	0	 (1.038)	 (2.441)	 (6.086)	 (6.583)	 (7.721)
	0.2	 (1.017)	 (2.322)	 (5.655)	 (6.197)	 (7.473)
	0.5	 (0.8853)	 (1.729)	 (3.848)	 (4.485)	 (5.979)
5	0	 (0.9748)	 (2.281)	 (5.675)	 (5.947)	 (7.203)
	0.2	 (0.9545)	 (2.170)	 (5.272)	 (5.598)	 (6.972)
	0.5	 (0.8290)	 (1.617)	 (3.476)	 (4.180)	 (5.566)

Fig. 7. Nodal patterns and $\omega(b^2/h)\sqrt{\rho_c/E_c}$ for cantilevered square moderately thick cracked Al/ZrO₂ FGM plate ($\hat{n} = 0, 5$, $d/b = 0, 0.2, 0.5$, $h/b = 0.1$, $c_y/b = 0.5$, $\alpha = 0^\circ$).

FGM plates with centrally positioned ($c_y/b = 0.5$) side cracks, oriented ($\alpha = 0^\circ$) parallel to the plate edges, the nodal patterns are either symmetric or anti-symmetric to the horizontal axis of the plate.

What can also be seen in Fig. 5 for a simply-supported moderately thick plate ($h/b = 0.1$) is that a side crack destroys any modal symmetry about the vertical central line. A shallow crack (i.e., $d/a = 0.2$) causes an unappreciable change in the first three longitudinal flexure nodal patterns from those for an intact plate, but the small crack does cause an appreciable change in the $\omega(b^2/h)\sqrt{\rho_c/E_c}$. The primary difference shows up more clearly for mode 5 of a deeply cracked ($d/a = 0.5$) thick simply-supported FGM plate, where an in-plane mode 5 with no crack, shifts to a distorted flexural mode 5. As expected, a deep side crack (i.e., $d/a = 0.5$) results in decreasing values of $\omega(b^2/h)\sqrt{\rho_c/E_c}$ for all modes of the simply-supported FGM thick plates analyzed. This is contrast with how in the cantilevered moderately thick plate ($h/b = 0.1$) (Fig. 6), the presence of a side crack on the symmetric axis does not change the symmetry of mode shapes with respect to the horizontal central line, and that indeed a deep side crack

(i.e., $d/a = 0.5$) does not cause the nodal patterns of the first two modes to be considerably different from those for an intact plate. The distinction here shows up more visibly for modes 4 and 5 of a deeply horizontally cracked ($d/a = 0.5$) thick cantilevered FGM plate, where an in-plane mode 4 and chordwise flexure mode 5 of an intact thick plate, shifts to a distorted predominately second torsion mode 4 coupled with longitudinal flexure and an in-plane mode 5. Again, a deep side crack (i.e., $d/a = 0.5$) results in decreasing values of $\omega(b^2/h)\sqrt{\rho_c/E_c}$ for all modes of the cantilevered FGM thick plates studied. Charted in Fig. 7 are nodal patterns and $\omega(b^2/h)\sqrt{\rho_c/E_c}$ for cantilevered cracked Al/ZrO₂ FGM square moderately thick plates ($\hat{n} = 0, 5$, $d/b = 0, 0.2, 0.5$, $h/b = 0.1$, $c_x/a = 0.5$, $\alpha = 90^\circ$), where a vertical side crack destroys the symmetry with respect to the horizontal central line and causes significantly distorted nodal patterns from those shown in Fig. 6, especially for the cases with large side cracks or the higher modes. The dissimilarity shows up most noticeably for modes 3 and 4 of a deeply vertically cracked ($d/b = 0.5$) thick cantilevered FGM plate, where an in-plane mode 4 and a distorted predominately second longitudinal flexure mode 3 of an intact thick plate, switches in modal

position to an in-plane mode 3 and a distorted predominately second longitudinal flexure mode 4.

5. Concluding remarks

Free vibrations of an FGM functionally graded plate with a side crack is investigated using the Ritz method. Upon briefly summarizing available Henchy–Mindlin, Reissner, and Ambartsumyan shear deformable plate theory approaches, Reddy’s third-order plate theory is adopted to model the free vibrations of an FGM plate. The Reddy approach used is a tradeoff between assumed displacement approximation complexity and sufficient transverse shear strain adequacy. To obtain accurate numerical solutions, a set of crack functions is proposed as the admissible functions in the Ritz method to properly account for the singularity behaviors in the neighborhood of the crack tip and to elucidate the discontinuities of displacements and slopes across the crack. What may be deficient computationally from the orthogonal polynomial displacement fields used is more than accounted for exactly through the use of the proposed crack functions, which model the singular behaviors of transverse normal and shear stresses at the tip of the side crack, and which account for the discontinuities of the displacements and their gradients across the crack. The use of the proposed set of functions to analyze the free vibrations of an FGM plate with a side crack was validated by performing comprehensive convergence studies. The results of the convergence studies agree very favorably with previously published solutions, confirming the validity and accuracy of the present solutions.

For the first time, accurate non-dimensional frequency data are provided for simply-supported square cracked Al/Al₂O₃ FGM thick plates and cantilevered rectangular cracked Al/ZrO₂ FGM thick plates. These plates have various material properties in the thickness direction, and have side cracks with various locations, orientations, and lengths. The numerical results support several important conclusions. Increasing the volume fraction exponent \hat{n} ($\hat{n} = 0.2, 1, 5,$ and 10) reduces the non-dimensional frequencies of Al/Al₂O₃ FGM plates, but not those of Al/ZrO₂ FGM plates. Using the Mori–Tanaka scheme to describe the variations of

material properties in the thickness direction yields smaller values of non-dimensional frequencies than Eq. (10). Increasing the crack length reduces the non-dimensional frequencies of the side-cracked plates. The decrease in the first five non-dimensional frequencies due to a small crack ($d/a = 0.1$) is not significant.

Although only the vibrations of side-cracked rectangular plates have been studied herein, the proposed set of crack functions can be extended to three-dimensional elasticity-based formulations of cracked FGM thick elastic bodies, and the crack functions can also be used directly for plates and thick elastic bodies with other geometries, such as circular, elliptical, polygonal, trapezoidal or skew. Additional work by the authors on these follow-on problems is forthcoming. The proposed set of functions can also be used in numerical methods other than the Ritz method, such as the element-free Galerkin method and the spectral-based method.

Acknowledgements

This work reported herein was supported by the National Science Council, Taiwan through research Grant No. NSC97-2221-E-009-075-MY3. This support is gratefully acknowledged. We are also grateful to the National Center for High-performance Computing for computer time and facilities.

Appendix A. Summary of available shear deformable plate theories for FGM thick plate flexural bending free response and vibration frequencies

The assumptions made by Kirchhoff, establishing classical plate theories, assumed: (i) displacement components are small compared with the thickness of the plate (h/a (or h/b) = 0.05 or less, see Fig. 1), (ii) normals to the middle surface of the plate before deformation remain straight and normal to the middle surface after deformation, (iii) transverse normal strain is negligible, and (iv) transverse normal stress is small and negligible compared to the in-plane normal stresses. The effect of shear deformation increases significantly as the plate thickness increases relative to the plate characteristic length (h/a (or h/b) = 0.05 or greater, see

Table A.1.1
Summary of first-order shear deformable plate theories (FOSDPT).

FOSDPT theory	Transverse shear strain $\epsilon_{xz}, \epsilon_{yz}$	Transverse normal strain ϵ_z	FOSDPT variables	FOSDPT assumed displacement approximations	BC	Shear factor κ
Reissner [18]	Quadratic	0	$u_o, v_o, w_o, \beta_x, \beta_y$	$u(x,y,z,t) = u_o(x,y,t) + z\beta_x(x,y,t)$ $v(x,y,z,t) = v_o(x,y,t) + z\beta_y(x,y,t)$ $w(x,y,z,t) = w_o(x,y,t)$	5	5/6
Mindlin [19]	Constant	0	$u_o, v_o, w_o, \psi_x, \psi_y$	$u(x,y,z,t) = u_o(x,y,t) + z\psi_x(x,y,t)$ $v(x,y,z,t) = v_o(x,y,t) + z\psi_y(x,y,t)$ $w(x,y,z,t) = w_o(x,y,t)$	5	$\pi^2/12$
Narasimhamurthy [20]	Quadratic	Non-zero	$u_o, v_o, w_o, w_{o,x}, w_{o,y}, \theta_x, \theta_y$	$u(x,y,z,t) = u_o(x,y,t) - zw_{o,x}(x,y,t) + [z + (4z^3/3h^2)]\theta_x$ $v(x,y,z,t) = v_o(x,y,t) - zw_{o,y}(x,y,t) + [z + (4z^3/3h^2)]\theta_y$ $w(x,y,z,t) = w_o(x,y,t) + [vh/8(1-v)]\{[(4z^2/h^2) - 1]\nabla^2 w_o - [(4z^2/h^2) - (8z^2/h^2) - 5/6](\theta_x + \theta_y)\}$	7	None
Schmidt [21]	Quadratic	0	$u_o, v_o, w_o, w_{o,x}, w_{o,y}, \theta_x, \theta_y$	$u(x,y,z,t) = u_o(x,y,t) - zw_{o,x}(x,y,t) + (3/2)[z - (4z^3/3h^2)]\theta_x$ $v(x,y,z,t) = v_o(x,y,t) - zw_{o,y}(x,y,t) + (3/2)[z - (4z^3/3h^2)]\theta_y$ $w(x,y,z,t) = w_o(x,y,t)$	7	None
Levinson [22]	Quadratic	0	$u_o, v_o, w_o, \psi_x, \psi_y, \phi_x, \phi_y$	$u(x,y,z,t) = u_o(x,y,t) + z\psi_x(x,y,t) + z^3\phi_x(x,y,t)$ $v(x,y,z,t) = v_o(x,y,t) + z\psi_y(x,y,t) + z^3\phi_y(x,y,t)$ $w(x,y,z,t) = w_o(x,y,t)$	7	None
Ambartsumyan ^a [23]	Quadratic	0	$u_o, v_o, w_o, w_{o,x}, w_{o,y}, \psi, \phi$	$u(x,y,z,t) = u_o(x,y,t) - zw_{o,x}(x,y,t) + (J_{01}/G)\phi(x,y,t) + (z/G)X_1(x,y,t) + (z^2/2hG)X_2(x,y,t)$ $v(x,y,z,t) = v_o(x,y,t) - zw_{o,y}(x,y,t) + (J_{02}/G)\psi(x,y,t) + (z/G)Y_1(x,y,t) + (z^2/2hG)Y_2(x,y,t)$ $w(x,y,z,t) = w_o(x,y,t)$	7	None

^a $J_{01} = J_{02} = (z/2)[h^2/4 - z^2/3]$; $X_1(x,y) = 1/2[\sigma_{xz}(x,y,+h/2) - \sigma_{xz}(x,y,-h/2)]$; $X_2(x,y) = [\sigma_{xz}(x,y,+h/2) + \sigma_{xz}(x,y,-h/2)]$; $Y_1(x,y) = 1/2[\sigma_{yz}(x,y,+h/2) - \sigma_{yz}(x,y,-h/2)]$; $Y_2(x,y) = [\sigma_{yz}(x,y,+h/2) + \sigma_{yz}(x,y,-h/2)]$.

Table A.1.2
Summary of higher-order shear deformable plate theories (HOSDPT).

HOSDPT theory	Transverse shear strain $\epsilon_{xz}, \epsilon_{yz}$	Transverse normal strain ϵ_z	HOSDPT variables	HOSDPT assumed displacement approximations	BC	Shear factor κ
Iyengar et al. [24,25] (extended Reissner)	Fourth-order	Non-zero	$\beta_x, \beta_y, \theta_x, \theta_y, \phi_x, \phi_y, w_o, w_1, w_2$	$u(x,y,z,t) = u_o(x,y,t) + z\beta_x(x,y,t) + z^2\theta_x(x,y,t) + z^3\phi_x(x,y,t)$ $v(x,y,z,t) = v_o(x,y,t) + z\beta_y(x,y,t) + z^2\theta_y(x,y,t) + z^3\phi_y(x,y,t)$ $w(x,y,z,t) = w_o(x,y,t) + zw_1(x,y,t) + z^2w_2(x,y,t)$	9	None
Kuznetov et al. [26]	Variable	Non-zero	$u_o, v_o, w_o, \psi_x, \psi_y, \psi_z$	$u(x,y,z,t) = u_o(x,y,t) + f_1(z)\psi_x(x,y,t)$ $v(x,y,z,t) = v_o(x,y,t) + f_2(z)\psi_y(x,y,t)$ $w(x,y,z,t) = w_o(x,y,t) + f_3(z)\psi_z(x,y,t)$	6	None
Vlasov [27]	Variable (Maclaurin Series)	Non-zero	u_o, v_o, w_o	$u(x,y,z,t) = u_o(x,y,t) + z[u_{,x}(x,y,t)]_o + (z^2/2)[u_{,xx}(x,y,t)]_o + \dots$ $v(x,y,z,t) = v_o(x,y,t) + z[v_{,x}(x,y,t)]_o + (z^2/2)[v_{,xx}(x,y,t)]_o + \dots$ $w(x,y,z,t) = w_o(x,y,t) + z[w_{,x}(x,y,t)]_o + (z^2/2)[w_{,xx}(x,y,t)]_o + \dots$	Series	None
Krishna-Murty I ^a [28–31]	Series	0	$u_o, v_o, w_o, w_{o,x}, w_{o,y}, \phi_n, \psi_n$	$u(x,y,z,t) = u_o(x,y,t) - zw_{o,x}(x,y,t) + A_n$ $v(x,y,z,t) = v_o(x,y,t) - zw_{o,y}(x,y,t) + B_n$ $w(x,y,z,t) = w_o(x,y,t)$	Series	None
Krishna-Murty II [28–31]	Fourth-order	0	$u_o, v_o, \beta_x, \beta_y, \theta_x, \theta_y, \phi_x, \phi_y, w_o, w_1, w_2$	$u(x,y,z,t) = u_o(x,y,t) + z\beta_x(x,y,t) + z^2\theta_x(x,y,t) + z^3\phi_x(x,y,t)$ $v(x,y,z,t) = v_o(x,y,t) + z\beta_y(x,y,t) + z^2\theta_y(x,y,t) + z^3\phi_y(x,y,t)$ $w(x,y,z,t) = w_o(x,y,t) + zw_1(x,y,t) + z^2w_2(x,y,t)$	11	None
Krishna-Murty III [28–31]	Eighth-order	0	$u_o, v_o, w_o, \phi_x, \psi_x, \phi_y, \psi_y, \theta_x, \theta_y$	$u(x,y,z,t) = u_o(x,y,t) + z\psi_x(x,y,t) + z^2\phi_x(x,y,t) + z^3\theta_x(x,y,t)$ $v(x,y,z,t) = v_o(x,y,t) + z\psi_y(x,y,t) + z^2\phi_y(x,y,t) + z^3\theta_y(x,y,t)$ $w(x,y,z,t) = w_o(x,y,t)$	9	None
Krishna-Murty IV [28–31] Reddy [9,14,32,33].	Quadratic	0	$u_o, v_o, w_o, w_{o,x}, w_{o,y}, \psi_x, \psi_y$	$u(x,y,z,t) = u_o(x,y,t) + z[\psi_x - (4/3)(z/h)^2(\psi_x(x,y,t) + w_{o,x}(x,y,t))]$ $v(x,y,z,t) = v_o(x,y,t) + z[\psi_y - (4/3)(z/h)^2(\psi_y(x,y,t) + w_{o,y}(x,y,t))]$ $w(x,y,z,t) = w_o(x,y,t)$	7	None

^a $A_n = p_n(z)\phi_{xn}(x,y)$, ($n = 1, 2, \dots, N$); $B_n = p_n(z)\phi_{yn}(x,y)$, ($n = 1, 2, \dots, N$).

Table A.1.3
Summary of higher-order shear deformable plate theories (HOSDPT) applicable to discrete layer or FGM ceramic-metal plate systems.

HOSDPT-FGM theory ^a	Transverse shear strain $\epsilon_{xz}, \epsilon_{yz}$	Transverse normal strain ϵ_z	HOSDPT-FGM variables	HOSDPT-FGM assumed displacement approximations	BC	Shear factor κ
Kant [34]	Quadratic	Non-zero	$u_o, v_o, w_o, \beta_x, \beta_y, \theta_x, \theta_y, \theta_z$	$u(x,y,z,t) = u_o(x,y,t) + z\beta_x(x,y,t) + z^3\theta_x(x,y,t)$ $v(x,y,z,t) = v_o(x,y,t) + z\beta_y(x,y,t) + z^3\theta_y(x,y,t)$ $w(x,y,z,t) = w_o(x,y,t) + z^2\theta_z(x,y,t)$	8	None
Reddy ^b [9,14,32,33]	Quadratic	0	$u_o, v_o, w_o, \phi_x, \phi_y, w_{o,x}, w_{o,y}$	$u(x,y,z,t) = u_o(x,y,t) + z\phi_x(x,y,t) - (4z^3/3h^2)[\phi_x(x,y,t) + w_{o,x}(x,y,t)]$ $v(x,y,z,t) = v_o(x,y,t) + z\phi_y(x,y,t) - (4z^3/3h^2)[\phi_y(x,y,t) + w_{o,y}(x,y,t)]$ $w(x,y,z,t) = w_o(x,y,t)$	7	None
Whitney and Sun ^d [35,36]	Linear	Non-zero	$u_o, v_o, w_o, \psi_x, \psi_y, \psi_z, \phi_x, \phi_y$	$u(x,y,z,t) = u_o(x,y,t) + z\psi_x(x,y,t) + z^2/2\phi_x(x,y,t)$ $v(x,y,z,t) = v_o(x,y,t) + z\psi_y(x,y,t) + z^2/2\phi_y(x,y,t)$ $w(x,y,z,t) = w_o(x,y,t) + z\psi_z(x,y,t)$	8	$\pi^2/12, \pi^2/15$
Nelson and Lorch [37]	Linear	Non-zero	$u_o, v_o, w_o, \psi_x, \psi_y, \psi_z, \phi_x, \phi_y, \phi_z$	$u(x,y,z,t) = u_o(x,y,t) + z\psi_x(x,y,t) + z^2\phi_x(x,y,t)$ $v(x,y,z,t) = v_o(x,y,t) + z\psi_y(x,y,t) + z^2\phi_y(x,y,t)$ $w(x,y,z,t) = w_o(x,y,t) + z\psi_z(x,y,t) + z^2\phi_z(x,y,t)$	9	K_{ij} (varies)
Lo et al. [38,39]	Quadratic	Non-zero	$u_o, v_o, w_o, \psi_x, \psi_y, \psi_z, \phi_x, \phi_y, \phi_z, \theta_x, \theta_y$	$u(x,y,z,t) = u_o(x,y,t) + z\psi_x(x,y,t) + z^2\phi_x(x,y,t) + z^3\theta_x(x,y,t)$ $v(x,y,z,t) = v_o(x,y,t) + z\psi_y(x,y,t) + z^2\phi_y(x,y,t) + z^3\theta_y(x,y,t)$ $w(x,y,z,t) = w_o(x,y,t) + z\psi_z(x,y,t) + z^2\phi_z(x,y,t)$	11	None
Prokopov ^c [40]	Series	Non-zero	$u_o, v_o, w_o, u_1, v_1, w_1$	$u(x,y,z,t) = cu_o(x,y,t) - A_0zsD_x\theta_o(x,y,t) + su_1(x,y,t) - A_1zdD_x\theta_1(x,y,t)$ $v(x,y,z,t) = cv_o(x,y,t) - A_0zsD_y\theta_o(x,y,t) + sv_1(x,y,t) - A_1zdD_y\theta_1(x,y,t)$ $w(x,y,z,t) = cw_o(x,y,t) + A_0\lambda D_{xy}^2\theta_o(x,y,t) + sw_1(x,y,t) - A_1zs\theta_1(x,y,t)$	Series	None
Pagano and Soni [41]	Cubic	Non-zero	$u_o, v_o, w_o, \psi_x, \psi_y, \psi_z, \phi_z$	$u(x,y,z,t) = u_o(x,y,t) + z\psi_x(x,y,t)$ $v(x,y,z,t) = v_o(x,y,t) + z\psi_y(x,y,t)$ $w(x,y,z,t) = w_o(x,y,t) + z\psi_z(x,y,t) + z^2/2\phi_z(x,y,t)$	7	None

^a z-Coordinate is measured from the ceramic-metal interface of the FGM plate (see Fig. 1c).

^b Adopted in present study.

^c $A_0 = v/[2(v-2)]$; $A_1 = A_0/2$; $c = \cos z D_{xy}$; $s = \sin z D_{xy}$; $d = (s-zc)/D_{xy}$; $\theta_o = D_xu_o + D_yv_o + w_1$; $\theta_1 = D_xu_1 + D_yv_1 - D_{xy}w_o$.

^d Discrete layer theory: $u^k(x,y,z,t) = u_o(x,y,t) - z^k\psi_x^k(x,y,t)$; $v^k(x,y,z,t) = v_o(x,y,t) - z^k\psi_y^k(x,y,t)$; $w^k(x,y,z,t) = w_o(x,y,t)$.

Fig. 1). Classical Kirchhoff plate theory underestimates flexural displacement solutions and overestimates flexural vibration solutions, mainly because thin-plate theory overestimates the flexural rigidity of the plate by neglecting its transverse shear flex-

ibility. This is the central justification of the vast amount of published literature [18–41] of alternative plate theories that provide more precise effects of transverse shear strains and normal strains for thick plate bending and vibrations problems.

First-order shear deformable plate theories (FOSDPT) [18–23] (as contrasted in Table A.I.1) replace the above classical Kirchhoff assumption (ii), that is, normals to the middle surface of the plate before deformation either remain straight (but not necessarily normal) to the middle surface after deformation, or in some theories, remain neither straight nor normal after deformation. The literature documents three approaches employed by researchers in developing FOSDPT approximations of FGM thick plates. The Reissner approach, as one, assumes a mixed in-plane normal and shear stress-displacement field. The Henchy–Mindlin approach, second, assumes a displacement field, whereas the Ambartsumyan approach, third, assumes an in-plane normal and shear stress field. Higher-order shear deformable plate theories (HOSDPT) (as put side-by-side in Table A.I.2) relax the Kirchhoff assumptions, as follows: (i) displacement components are small compared with the thickness of the plate; (ii) normals to the midsurface of the FGM plate before deformation which are straight are not necessarily normal nor straight after deformation; (iii) transverse normal strain is not negligible; (iv) transverse normal stresses generally are not negligible. Only the first Kirchhoff assumption (i) is retained, which is required for the HOSDPT approaches to be linear. The HOSDPT assumptions (iii) and (iv) are seen to be changed from those of the FOSDPT approaches. The literature documents Reissner, Henchy–Mindlin, and Ambarsumyan HOSDPT approaches [24–33], as compared in Table A.I.2. The present Reddy HOSDPT approached adopted in this study (Eqs. (1)) is a Henchy–Mindlin-based approach, which corrects upon a similar Henchy–Mindlin approach of Kant by subtracting cubic-order terms through the FGM plate thickness proportional to sums of first-order bending rotations and transverse normal strains.

Both FOSDPT and HOSDPT approaches, when applied to discrete layer or FGM thick plate systems [34–41] (see Table A.I.3), consider the assumed displacement approximation as smeared over the plate thickness and evaluate the effective stiffness and mass of the entire FGM thick plate in terms of the stiffness and mass of the material layers. One drawback is these approaches give inadequate stresses, although they are typically sufficiently accurate for flexural bending and vibration frequency solutions, mainly because the assumed displacements are continuous across the FGM plate thickness, whereas the displacement gradients or transverse shear and normal stresses may be discontinuous at the material interface of the FGM plate. Some shear deformable discrete layer thick plate researchers have assumed displacement approximations over each material layer separately, while ensuring the displacements satisfy the continuity conditions at the interface of the two material layers.

Table A.I.3 contrasts the various assumed displacement approximations and resulting transverse normal and shear strain approximations resulting from them. The Reddy HOSDPT approach adopted in the present study is a somewhat compromise tradeoff between assumed displacement approximation complexity and sufficient transverse shear strain adequacy. What may be deficient computationally from the orthogonal polynomial displacement fields used in the present Ritz procedure, in the ideal sense, is more than accounted for exactly through the use of the proposed crack functions, which model the singular behaviors of transverse normal and shear stresses at the tip of the side crack and which account for the discontinuities of the displacements and their gradients across the crack. It is advantageous in the present Ritz procedure that a hybrid set of trial functions be used so that it constitutes not only an orthogonal set, but also that it incorporates a set of crack functions derived from the exact solution in the vicinity of the tip of a side crack, which may be used to computational advantage in achieving a robust upper bound approximation on the exact solution of the titled vibration problem of cracked rectangular FGM thick plates. It is shown specifically in detail herein that

inclusion of these crack functions in the assumed displacement field – albeit addressing singular effects local to the tip of the side crack – do have a global effect on flexural bending free response and vibration frequency solutions of cracked FGM thick plates.

Appendix B. Stiffness and mass definitions of Eq. (9)

The expressions for components in stiffness and mass matrices in Eq. (9):

$$\begin{aligned}
 K_{ij}^{11} &= \iint \left\{ \bar{A}_{11} \xi_{i,x} \xi_{j,x} + \bar{A}_{44} \xi_{i,y} \xi_{j,y} \right\} dA, & K_{ij}^{12} &= \iint \left\{ \bar{A}_{12} \xi_{i,x} \xi_{j,y} + \bar{A}_{44} \xi_{i,y} \xi_{j,x} \right\} dA, \\
 K_{ij}^{13} &= \iint \left\{ \bar{K}_{11} \xi_{i,x} \eta_{j,x} + \bar{K}_{44} \xi_{i,y} \eta_{j,y} \right\} dA, & K_{ij}^{14} &= \iint \left\{ \bar{K}_{12} \xi_{i,x} \chi_{j,y} + \bar{K}_{44} \xi_{i,y} \chi_{j,x} \right\} dA, \\
 K_{ij}^{15} &= \iint \left\{ \xi_{i,x} C_1 (-\bar{E}_{11} \varphi_{j,xx} - \bar{E}_{12} \varphi_{j,yy}) - 2C_1 \bar{E}_{44} \xi_{i,y} \varphi_{j,xy} \right\} dA, \\
 K_{ij}^{22} &= \iint \left\{ \bar{A}_{11} \xi_{i,y} \xi_{j,y} + \bar{A}_{44} \xi_{i,x} \xi_{j,x} \right\} dA, & K_{ij}^{23} &= \iint \left\{ \bar{K}_{12} \xi_{i,y} \eta_{j,x} + \bar{K}_{44} \xi_{i,x} \eta_{j,y} \right\} dA, \\
 K_{ij}^{24} &= \iint \left\{ \bar{K}_{11} \xi_{i,y} \chi_{j,y} + \bar{K}_{44} \xi_{i,x} \chi_{j,x} \right\} dA, \\
 K_{ij}^{25} &= \iint \left\{ -C_1 \bar{E}_{12} \xi_{i,y} \varphi_{j,xx} - C_1 \bar{E}_{11} \xi_{i,y} \varphi_{j,yy} - 2C_1 \bar{E}_{44} \xi_{i,x} \varphi_{j,xy} \right\} dA, \\
 K_{ij}^{33} &= \iint \left\{ (\bar{J}_{11} - C_1 \bar{L}_{11}) \eta_{i,x} \eta_{j,x} + (\bar{J}_{44} - C_1 \bar{L}_{44}) \eta_{i,y} \eta_{j,y} \right. \\
 &\quad \left. + (\bar{M}_0 - C_2 \bar{M}_2) \eta_i \eta_j \right\} dA, \\
 K_{ij}^{34} &= \iint \left\{ (\bar{J}_{12} - C_1 \bar{L}_{12}) \eta_{i,x} \chi_{j,y} + (\bar{J}_{44} - C_1 \bar{L}_{44}) \eta_{i,y} \chi_{j,x} \right\} dA, \\
 K_{ij}^{35} &= \iint \left\{ C_1 \eta_{i,x} (-\bar{L}_{11} \varphi_{j,xx} - \bar{L}_{12} \varphi_{j,yy}) - 2C_1 \bar{L}_{44} \eta_{i,y} \varphi_{j,xy} + (\bar{M}_0 - C_2 \bar{M}_2) \eta_i \varphi_{j,x} \right\} dA, \\
 K_{ij}^{44} &= \iint \left\{ (\bar{J}_{11} - C_1 \bar{L}_{11}) \chi_{i,y} \chi_{j,y} + (\bar{J}_{44} - C_1 \bar{L}_{44}) \chi_{i,x} \chi_{j,x} \right. \\
 &\quad \left. + (\bar{M}_0 - C_2 \bar{M}_2) \chi_i \chi_j \right\} dA, \\
 K_{ij}^{45} &= \iint \left\{ -C_1 \bar{L}_{12} \chi_{i,y} \varphi_{j,xx} - C_1 \bar{L}_{11} \chi_{i,y} \varphi_{j,yy} - 2C_1 \bar{L}_{44} \chi_{i,x} \varphi_{j,xy} + (\bar{M}_0 - C_2 \bar{M}_2) \chi_i \varphi_{j,y} \right\} dA, \\
 K_{ij}^{55} &= \iint \left\{ C_1^2 \bar{H}_{11} (\varphi_{i,xx} \varphi_{j,xx} + \varphi_{i,yy} \varphi_{j,yy}) + C_1^2 \bar{H}_{12} (\varphi_{i,xx} \varphi_{j,yy} + \varphi_{i,yy} \varphi_{j,xx}) \right. \\
 &\quad \left. + 4C_1^2 \bar{H}_{44} \varphi_{i,xy} \varphi_{j,xy} + (\bar{M}_0 - C_2 \bar{M}_2) (\varphi_{i,x} \varphi_{j,x} + \varphi_{i,y} \varphi_{j,y}) \right\} dA, \\
 M_{ij}^{11} &= \bar{\rho}_0 \iint \xi_i \xi_j dA, & M_{ij}^{12} &= 0, & M_{ij}^{13} &= (\bar{\rho}_1 - C_1 \bar{\rho}_3) \iint \xi_i \eta_j dA, \\
 M_{ij}^{14} &= 0, & M_{ij}^{15} &= (-C_1 \bar{\rho}_3) \iint \xi_i \varphi_{j,x} dA, & M_{ij}^{22} &= \bar{\rho}_0 \iint \xi_i \xi_j dA, \\
 M_{ij}^{23} &= 0, & M_{ij}^{24} &= (\bar{\rho}_1 - C_1 \bar{\rho}_3) \iint \xi_i \chi_j dA, & M_{ij}^{25} &= (-C_1 \bar{\rho}_3) \iint \xi_i \varphi_{j,y} dA, \\
 M_{ij}^{33} &= (\bar{\rho}_2 - 2C_1 \bar{\rho}_4 + C_1^2 \bar{\rho}_6) \iint \eta_i \eta_j dA, & M_{ij}^{34} &= 0, \\
 M_{ij}^{35} &= (-C_1 \bar{\rho}_4 + C_1^2 \bar{\rho}_6) \iint \eta_i \varphi_{j,x} dA, \\
 M_{ij}^{44} &= (\bar{\rho}_2 - 2C_1 \bar{\rho}_4 + C_1^2 \bar{\rho}_6) \iint \chi_i \chi_j dA, & M_{ij}^{45} &= (-C_1 \bar{\rho}_4 + C_1^2 \bar{\rho}_6) \iint \chi_i \varphi_{j,y} dA, \\
 M_{ij}^{55} &= C_1^2 \bar{\rho}_6 \iint (\varphi_{i,x} \varphi_{j,x} + \varphi_{i,y} \varphi_{j,y}) dA + \bar{\rho}_0 \iint \varphi_i \varphi_j dA,
 \end{aligned}$$

where $\bar{\rho}_i = \int_{-h/2}^{h/2} \rho(z) z^i dz$.

References

- [1] Koizumi M. The concept of FGM. In: Holt JB et al., editors. Functionally gradient materials. Westerville, OH: The American Ceramic Society; 1993. p. 3–10.
- [2] Nogata F. Learning about design concepts from natural functionally graded materials. In: Jones W et al., editors. The composites and functionally graded materials. NY: American Society of Mechanical; 1997. p. 11–8.
- [3] Niino M, Maeda S. Recent development status of functionally gradient materials. ISIJ Intl 1990;30:699–703.
- [4] Noda N. Thermal stresses in materials with temperature-dependent properties. Appl Mech Rev 1991;44:383–97.
- [5] Tanigawa Y. Some basic thermoelastic problems for non-homogeneous structural materials. Appl Mech Rev 1995;48:377–89.
- [6] Yang Y, Shen HS. Dynamic response of initially stressed functional graded rectangular thin plates. Compos Struct 2001;54:497–508.
- [7] He XQ, Ng TY, Sivashanker S, Liew KM. Active control of FGM plates with integrated piezoelectric sensors and actuators. Intl J Solids Struct 2001;38:1641–55.
- [8] Zhao X, Lee YY, Liew KM. Free vibration analysis of functionally graded plates using the element-free kp-Ritz method. J Sound Vib 2009;319:918–39.
- [9] Reddy JN. Analysis of functionally graded plates. Int J Numer Method Eng 2000;47(1–3):663–84.

- [10] Ferreira AJM, Batra RC, Roque CMC, Qian LF, Jorge RMN. Natural frequencies of functionally graded plates by a meshless method. *Compos Struct* 2006;75:593–600.
- [11] Matsunaga H. Free vibration and stability of functionally graded plates according to a 2-D higher-order deformation theory. *Compos Struct* 2008;82:499–512.
- [12] Qian LF, Batra RC, Chen LM. Static and dynamic deformations of thick functionally graded elastic plates by using higher-order shear and normal deformable plate theory and meshless local Petrov–Galerkin method. *Composites: Part B* 2004;35:685–97.
- [13] Vel SS, Batra RC. Three-dimensional exact solution for the vibration of functionally graded rectangular plates. *J Sound Vib* 2004;272(3):703–30.
- [14] Reddy JN. *Theory and analysis of elastic plates*. Philadelphia, PA: Taylor & Francis; 1999.
- [15] Huang CS, Chang MJ. Geometrically induced stress singularities of a thick FGM plate based on the third-order shear deformation theory. *Mech Adv Mater Struct* 2009;16(2):83–97.
- [16] Huang CS, Leissa AW. Vibration analysis of rectangular plates with side cracks via the Ritz method. *J Sound Vib* 2009;323(3–5):974–88.
- [17] Ritz W. Über eine neue Methode zur Lösung gewisser Variationsprobleme der mathematischen Physik. *Journal für Reine und Angewandte Mathematik* 1908;135:1–61.
- [18] Reissner E. On the analysis of first and second order shear deformation effects for isotropic elastic plates. *ASME J Appl Mech* 1980;47:959–61.
- [19] Mindlin RD. Influence of rotatory inertia and shear on flexural motions of isotropic elastic plates. *ASME J Appl Mech* 1951;73:31–8.
- [20] Narasimhamurthy P. The effect of transverse shear deformation and rotary inertia in wave propagation and vibration of thin elastic plates. In: *Proceedings of the 3rd congressional theoretical applied mechanics*, Bangalore, India, Indian Society of Theoretical Applied Mechanics, Indian Institute of Technology, Kharagpur; 1957. p. 351–60.
- [21] Schmidt R. A refined nonlinear theory of plates with transverse shear deformation. *Indust Math* 1977;27(1):23–38.
- [22] Levinson M. An accurate simple theory of the statics and dynamics of elastic plates. *Mech Res Commun* 1980;7(6):343–50.
- [23] Ambartsumyan SA. *Theory of anisotropic plates*. Technomic Stanford; 1970.
- [24] Iyengar KTSR, Pandya SK. Vibration of orthotropic rectangular thick plates. *Int J Struct* 1982;2(4):149–56.
- [25] Iyengar KTSR, Chadrashekhara K, Sebastian VK. On the analysis of thick rectangular plates. *Z Angew Math Mech* 1974;54(9):589–91.
- [26] Kuznetsov ND, Kartashov GG, et al. Natural vibrational modes of laminated anisotropic plates and flat shells. *Soviet Appl Mech* 1981;17(4):334–9.
- [27] Vlasov VZ. The method of initial function in problems of theory of thick plates and shells. In: *Ninth congress of international mechanical applications*, vol. 6, University of Bruxelles; 1957. p. 321–30.
- [28] Krishna Murty AV. Higher-order theory for vibrations of thick plates. *AIAA J* 1977;15(12):1823–4.
- [29] Krishna Murty AV. Toward of consistent plate theory. *AIAA J* 1986;24(6):1047–8.
- [30] Krishna Murty AV. Flexural of composite plates. *Compos Struct* 1987;7:161–77.
- [31] Krishna Murty AV, Vellaichamy S. On higher-order shear deformation theory of laminated composite panels. *Compos Struct* 1987;8:247–70.
- [32] Reddy JN. A simple higher-order theory for laminated composite plates. *ASME J Appl Mech* 1984;51:745–52.
- [33] Reddy JN, Phan ND. Analysis of laminated composite plates using a higher-order shear deformation theory. *Int J Numer Methods Eng* 1985;21:2201–19.
- [34] Kant T. Numerical analysis of thick plates. *Comput Methods Appl Mech Eng* 1982;31(1):1–18.
- [35] Sun CT, Whitney JM. Theories for dynamic response of laminated plates. *AIAA J* 1973;11:178–83.
- [36] Whitney JM, Sun CT. A higher-order theory for extensional motion of laminated composites. *J Sound Vib* 1973;30:85–97.
- [37] Nelson RB, Lorch DR. A refined theory for laminated orthotropic plates. *ASME J Appl Mech* 1974;E41(1):177–83.
- [38] Lo KH, Christensen RM, Wu EM. A high-order theory of plate deformation. Part I: homogeneous plates. *ASME J Appl Mech* 1977;44:663–8.
- [39] Lo KH, Christensen RM, Wu EM. A high-order theory of plate deformation. Part II: laminated plates. *ASME J Appl Mech* 1977;44:669–76.
- [40] Prokopov VK. Application of the symbolic method to the derivation of the equations of the theory of plates. *J Appl Math Mech* 1965;29(5):1064–83.
- [41] Pagano NJ, Soni SR. Global–local laminate variational model. *Int J Solids Struct* 1983;19:207–28.
- [42] Alghothani A. A unified approach to the dynamic analysis of bending and extension of moderately thick laminated composite plates. Ph.D. Dissertation, Ohio State University; 1986.
- [43] Hanna NF. Thick plate theory with application to vibration. Ph.D. Dissertation, Ohio State University; 1990.
- [44] Bhat RB. Natural frequencies of rectangular plates using characteristic orthogonal polynomials in Rayleigh–Ritz method. *J Sound Vib* 1985;102(4):493–9.
- [45] Mori T, Tanaka K. Average stress in matrix and average elastic energy of material with misfitting inclusions. *Acta Metall* 1973;21:571–4.
- [46] Benveniste Y. A new approach to the application of Mori–Tanaka's theory of composite materials. *Mech Mater* 1987;6:147–57.
- [47] Stahl B, Keer LM. Vibration and stability of cracked rectangular plates. *Int J Solids Struct* 1972;8(1):69–91.